

# Bulk-Boundary Correspondence in a Non-Hermitian System in One Dimension with Chiral-Inversion Symmetry

L. Jin<sup>1,\*</sup> and Z. Song<sup>1</sup>

<sup>1</sup>*School of Physics, Nankai University, Tianjin 300071, China*

Asymmetric coupling amplitudes effectively create an imaginary gauge field, which induces a non-Hermitian Aharonov-Bohm (AB) effect. Nonzero imaginary magnetic flux invalidates the bulk-boundary correspondence and leads to a topological phase transition. However, the way of non-Hermiticity appearance may alter the system topology. By alternatively introducing the non-Hermiticity under symmetry to prevent nonzero imaginary magnetic flux, the bulk-boundary correspondence recovers and every bulk state becomes extended; the bulk topology of Bloch Hamiltonian predicts the (non)existence of edge states and topological phase transition. These are elucidated in a non-Hermitian Su-Schrieffer-Heeger model, where chiral-inversion symmetry ensures the vanishing of imaginary magnetic flux. The average value of Pauli matrices under the eigenstate of chiral-inversion symmetric Bloch Hamiltonian defines a vector field, the vorticity of topological defects in the vector field is a topological invariant. Our findings are applicable in other non-Hermitian systems. We first uncover the roles played by non-Hermitian AB effect and chiral-inversion symmetry for the breakdown and recovery of bulk-boundary correspondence, and develop new insights for understanding non-Hermitian topological phases of matter.

*Introduction.*—Topological theory has been well established in condensed matter physics [1–32] and recent experimental progresses in optics boost the development of topological photonics [33–41]. The existence of gapless edge states of a system under open boundary condition (OBC) is predictable from the change of topological invariants associated with the bulk topology of system under periodical boundary condition (PBC), known as the (conventional) bulk-boundary correspondence, which is ubiquitously applicable in Hermitian systems.

In parallel, non-Hermitian physics exhibits considerable intriguing features [42–75]; the unexpected novel interface states appear between non-Hermitian periodic media with distinct topologies [76–89]. These stimulate the studies of topological phases and edge states in non-Hermitian systems [90–117]. Non-Hermitian band theory and the topological characterization are developed employing the left and right eigenstates [48, 52]; the Chern number, generalized Berry phase and winding numbers are quantized as topological invariants [107–109].

Remarkably, the bulk-boundary correspondence [118] is invalid in certain non-Hermitian topological systems [119–121]: Systems under PBC and OBC have dramatically different energy spectra, and all the eigenstates localize near system boundaries (the non-Hermitian skin effect) [122–124]. These have received great research interests in non-Hermitian systems of asymmetric Su-Schrieffer-Heeger (SSH) model, topological insulators, and nodal-line semimetals [122–131]. Biorthogonal [122] and non-Bloch bulk-boundary correspondences [123] are suggested. In contrast, non-Hermiticity does not inevitably destroy the bulk-boundary correspondence [77, 78, 93–97], which is verified in a parity-time-symmetric non-Hermitian SSH model with staggered couplings and losses [85–92]. Questions arise: Why bulk-boundary correspondence fails in certain non-Hermitian systems?

What roles do non-Hermiticity and symmetry play in the breakdown of bulk-boundary correspondence? How to characterize the topological properties and understand the topological invariant without (conventional) bulk-boundary correspondence?

In this Rapid Communication, we first report that *chiral-inversion symmetry plays an important role* for the bulk-boundary correspondence in non-Hermitian system of a non-Hermitian SSH model with asymmetric coupling; which leads to a *non-Hermitian Aharonov-Bohm (AB) effect* with an imaginary magnetic flux under PBC and a non-Hermitian skin effect under OBC without chiral-inversion symmetry. The imaginary magnetic flux results in complex spectrum and a topological phase transition, but it disappears under OBC; the OBC spectrum significantly differs from the PBC spectrum, and the bulk-boundary correspondence fails. Non-Hermitian AB effect vanishes if the asymmetry is alternatively introduced without breaking chiral-inversion symmetry. The bulk-boundary correspondence is valid; a topological invariant is constructed from the system bulk with the imaginary gauge field removed, being the vorticity of band touching points as topological defects in the vector field defined from the average values of Pauli matrices. Our findings are valid for other non-Hermitian topological systems.

*Topological phase transition induced by symmetry breaking.*—The Bloch Hamiltonian of a non-Hermitian system  $a$  (Fig. 1) under PBC is

$$H_a(k) = (t_1 + t_2 \cos k) \sigma_x + (t_2 \sin k - i\gamma) \sigma_y, \quad (1)$$

where  $\sigma_{x,y}$  are the Pauli matrices.  $t_2$  is the intercell coupling. Set  $\mu = t_1 - \gamma$  and  $\nu = t_1 + \gamma$ , the asymmetric intracell coupling amplitude ( $\mu \neq \nu^*$ ) raises the non-Hermiticity. Non-Hermitian asymmetric coupling can be realized between primary resonators evanescently cou-

pled through auxiliary resonator [132–134], which has half perimeter gain and half perimeter loss, leading to the amplification and attenuation for the coupling amplitudes in opposite tunneling directions. Implementation of asymmetric coupling with ultracold atoms in optical lattice is possible [124].

In Hermitian case ( $\gamma = 0$ ), system  $a$  holds chiral-inversion symmetry

$$(\mathcal{SP}) H_a(k) (\mathcal{SP})^{-1} = -H_a(-k), U_{\mathcal{SP}} H_a U_{\mathcal{SP}}^{-1} = -H_a. \quad (2)$$

The constraints are for a *combined* chiral-inversion symmetry.  $\mathcal{SP}$  and  $U_{\mathcal{SP}}$  are unitary operators.  $H_a$  [ $H_a(k)$ ] is the Hamiltonian in the real-space ( $k$ -space). Two band touching degeneracy points exist [Fig 2(d)].

In non-Hermitian case ( $\gamma \neq 0$ ), unlike the alternative gain and loss [86–92], the asymmetric coupling breaks the chiral-inversion symmetry ( $H_a$  in Fig. 1). Taken  $\mu\nu > 0$  as illustration (see Supplemental Material A [135]) and rewritten

$$\mu = \sqrt{\mu\nu} e^{-\phi}, \nu = \sqrt{\mu\nu} e^{\phi}, \quad (3)$$

where  $e^{-\phi} \equiv \sqrt{\mu/\nu}$  [133, 134, 136], the asymmetric coupling is expressed as a symmetric coupling  $\sqrt{\mu\nu}$  with Peierls “phase” factor [37–41, 137–143] of amplification/attenuation  $e^{\pm\phi}$  [144], which indicates the presence of an imaginary gauge field [132–134]. A non-Hermitian AB “phase” factor of amplification/attenuation  $e^{\pm i(2n\phi)}$  is accumulated when particle circling a loop in  $H_a$  under PBC; where  $2n\phi$  is the imaginary magnetic flux [140–

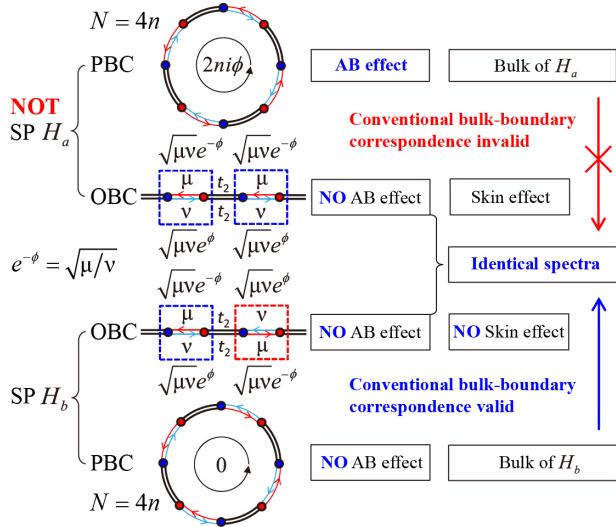


FIG. 1. Breakdown (recovery) of bulk-boundary correspondence for system without (with) chiral-inversion symmetry from the viewpoint of non-Hermitian AB effect. Imaginary gauge field induces nonzero (zero) imaginary magnetic flux in  $H_a$  ( $H_b$ ) under PBC. Topological invariant obtained from the bulk Bloch Hamiltonian of system  $b$  is a Bloch (non-Bloch) topological invariant for system  $b$  (a). Lattice size is  $N = 4n$ .

144]. The eigenvalues are

$$E_{a,\pm} = \pm \sqrt{t_2^2 + \mu\nu + 2t_2\sqrt{\mu\nu} \cos(k + i\phi)}, \quad (4)$$

with  $k = \pi m/n$ , integer  $m \in [1, 2n]$  [Fig. 2(a)].

In contrast to a real magnetic flux that shifts  $k$  in the momentum space without varying the dispersion relation [140], the momentum changes to  $k + i\phi$  [125, 126, 129] and spectrum becomes fully complex affected by imaginary magnetic flux; which induces a topological phase transition with band touching degeneracy points split into pairs of band touching EPs [Figs. 2(a) and 2(d)] [71] that exhibit different topology [145–161]. Imaginary magnetic flux is absent under OBC, thus the spectra and band touching points under PBC [Fig. 2(a)] and OBC [Fig. 2(c)] are dramatically different [119–128]. The eigenstate amplitude is one-way enlarged under OBC because of imaginary gauge field [133, 134, 162]; and all the eigenstates localize at system boundary (non-Hermitian skin effect [123–127]). The localization length is  $\xi = \phi^{-1}$  [163]. The inverse participation ratio (IPR)  $\sum_j |\psi_j|^4 / (\sum_j |\psi_j|^2)^2$  of bulk states scales as  $N^{-1}$  for small  $N$ , particularly for weak non-Hermiticity; and becomes system size insensitive when the localization dominates at large  $N$  (see Supplemental Material B [135]).

*Bulk-boundary correspondence.*—Chiral-inversion symmetry holds when non-Hermiticity is alternatively introduced in system  $b$  ( $H_b$  in Fig. 1) [164]. Under symmetry protection, two degeneracy points move without splitting into EP pairs [Figs. 2(b) and 2(d)]. The eigenstates under OBC are symmetric/antisymmetric. All bulk states are extended and non-Hermitian skin effect disappears

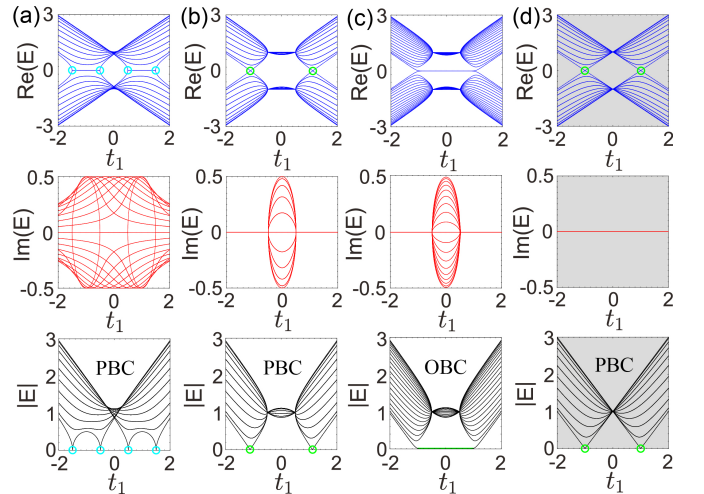


FIG. 2. (a) [(b)] Energy spectrum for  $H_a$  ( $H_b$ ) under PBC. (c) Identical spectra of  $H_a$  and  $H_b$  under OBC with one intercell coupling  $t_2$  missing, and (d)  $H_a$  and  $H_b$  under PBC in the Hermitian case ( $\gamma = 0$ ). The band touching exceptional points (degeneracy points) are indicated by the cyan (green) hollow circles. The system parameters are  $N = 40$ ,  $t_2 = 1$ , and  $\gamma = 1/2$  in (a-c).

even most bulk states have complex eigenvalues (IPR of bulk states of system  $b$  is inversely proportional to the system size [135]). Although the significant difference between eigenstates, systems  $a$  and  $b$  under OBC possess *identical* energy spectra (see Supplemental Material C [135]), the imaginary gauge fields do not affect OBC spectra [Fig. 2(c)]. These manifest that *the way of non-Hermiticity appearance affects system topology*. In particular, the *non-Hermiticity solely induces nontrivial topology* at  $t_1 = t_2$  [165].

The amplification and attenuation cancel in  $H_b$ . The combined chiral-inversion ( $\mathcal{SP}$ ) symmetry prevents the appearance of nonzero imaginary magnetic flux and the bulk-boundary correspondence is valid [Figs. 2(b) and 2(c)] (also in Refs. [77, 78, 86–94], but is invalid in Refs. [119–130] without chiral-inversion symmetry), while *individual* chiral and inversion symmetries are not necessarily hold separately (see Supplemental Material D [135]). The (non)existence of topologically protected edge states is predictable from the bulk of system  $b$ ,

$$H_b(k) = \begin{pmatrix} 0 & \sqrt{\mu\nu}e^{-\phi} & 0 & t_2e^{-ik} \\ \sqrt{\mu\nu}e^{\phi} & 0 & t_2 & 0 \\ 0 & t_2 & 0 & \sqrt{\mu\nu}e^{\phi} \\ t_2e^{ik} & 0 & \sqrt{\mu\nu}e^{-\phi} & 0 \end{pmatrix}. \quad (5)$$

Through a similar transformation with only nonzero diagonal elements  $U_{\mu\nu} = \text{diag}(\sqrt{\nu}, \sqrt{\mu}, \sqrt{\mu}, \sqrt{\nu})$ , the imaginary gauge fields (factors  $e^{\pm\phi}$ ) are removed from  $H_b$  (see Supplemental Material E [135]); and we obtain  $U_{\mu\nu}H_b(k)U_{\mu\nu}^{-1}$ , which is equivalent to a two-site unit cell bulk  $h_b(k) = (\sqrt{\mu\nu} + t_2 \cos k)\sigma_x + (t_2 \sin k)\sigma_y$ . The eigenvalues are

$$E_{b,\pm} = \pm\sqrt{t_2^2 + \mu\nu + 2t_2\sqrt{\mu\nu}\cos(k)}, \quad (6)$$

where  $k = \pi m/n$ ,  $m \in [1, 2n]$ . The bulk topology of  $h_b(k)$  correctly predicts the (non)existence of edge states in both systems  $a$  and  $b$  under OBC (Fig. 1) [135]. Removing the imaginary gauge field in system bulk gives  $h_b(k)$ , which is identical with that found by solving the open system [123].

For  $\gamma = |r|e^{i\theta}$  ( $-\pi \leq \theta \leq \pi$ ), the band gap closes at

$$(t_1^2 - |r|^2)^2 + 4t_1^2|r|^2\sin^2\theta = t_2^4, \quad (7)$$

and  $\cos^2(k) = [t_2^2 + t_1^2 - |r|^2\cos(2\theta)]/(2t_2^2)$ . The finite size effects appear in discrete systems (see Supplemental Material F [135]). For real  $\mu$  and  $\nu$  at  $\theta = 0$ , the band touching points are degeneracy (exceptional) points at  $t_1^2 = +(-)t_2^2 + \gamma^2$  [122, 123], being topological defects carrying integer (half-integer) vorticity. The band touching EPs only appear for  $\gamma^2 > t_2^2$ .

*Topological invariant.*—Topology invariants are recently constructed in non-Hermitian systems [94, 107–109, 112, 123]. The Chern number defined via Berry curvature [94, 108], the vorticity defined via the complex

energy [109], and the generalized Berry phase defined via the argument of effective magnetic field [107, 108, 112] are quantized. The vorticity of topological defects in a vector field  $\mathbf{B}(\mathbf{k})$  associated with the Bloch Hamiltonian is a topological invariant [166, 167]; we generalize this vorticity to non-Hermitian systems through defining a two-component vector field  $\mathbf{F}(\mathbf{k}) = (\langle\sigma_x\rangle, \langle\sigma_y\rangle)$  [Figs. 3(a) and 3(b)] that is composed by the average values of Pauli matrices under the eigenstates of  $h_b(k)$ .  $w = \oint_L (2\pi)^{-1} (\hat{F}_x \nabla \hat{F}_y - \hat{F}_y \nabla \hat{F}_x) d\mathbf{k}$  characterizes the vorticity of topological defects inside the loop  $L$  in the parameter plane  $\mathbf{k} = (k, t_2)$ , where  $\hat{F}_{x(y)} = F_{x(y)}/\sqrt{F_x^2 + F_y^2}$  and  $\nabla = \partial/\partial\mathbf{k}$ , which is in accord with that defined in the Brillouin zone of a two-dimensional (2D) brick wall lattice (see Supplemental Material E [135]). The varying direction of  $\mathbf{F}(\mathbf{k})$  accumulated is  $2\pi w = \pm 2\pi$  ( $\pm\pi$ ) in Fig. 3(a) [Fig. 3(b)] if  $L$  encircles a topological defect, the plus (minus) sign corresponds to the vortex (antivortex); otherwise, if  $L$  does not encircle a topological defect, the varying direction is  $2\pi w = 0$ .

Phase diagram is plotted in Fig. 3(c) for real  $\gamma$ . For  $\mu\nu > 0$ , the degeneracy points are at  $t_2^2 - \mu\nu = 0$ . As non-Hermiticity increases, the band gap inside two EPs

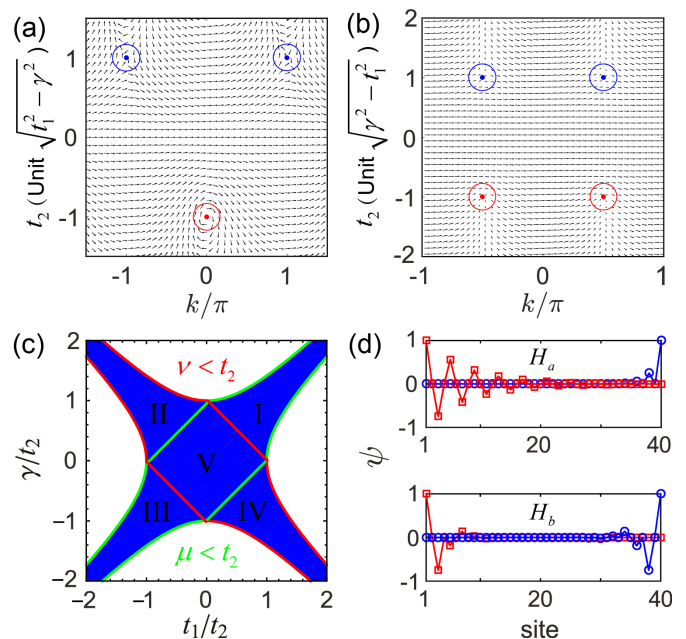


FIG. 3. Vector field  $\mathbf{F}(\mathbf{k}) = (\langle\sigma_x\rangle, \langle\sigma_y\rangle)$  associated with  $E_{b,+}$  of  $h_b(k)$  for (a)  $\mu\nu = t_1^2 - \gamma^2 > 0$  and (b)  $\mu\nu = t_1^2 - \gamma^2 < 0$ . Red (blue) circles indicate the topological defects with vortices (antivortices), which appear at  $(k, t_2) = (0, -\sqrt{t_1^2 - \gamma^2})$  or  $(\pm\pi, \sqrt{t_1^2 - \gamma^2})$  in (a) and at  $(k, t_2) = (\pm\pi/2, \pm\sqrt{\gamma^2 - t_1^2})$  in (b). (c) Phase diagram for real  $\gamma$ . Two topological zero edge states exist in the blue region  $-t_2^2 < \mu\nu < t_2^2$  for one intercell coupling  $t_2$  missing. (d) Zero edge states for systems  $a$  and  $b$  under OBC. The system parameters are  $N = 40$ ,  $t_1 = 1/4$ ,  $\gamma = 1/2$ , and  $t_2 = 1$ .

[48, 74, 75] with complex spectrum diminishes and closes at  $t_1 = 0$  when  $\gamma^2 = t_2^2$ .  $\mu\nu = 0$  ( $t_1 = \pm\gamma$ ) are EPs, where the eigenstates are highly defective and fully constituted by two-state coalescences at energy  $\pm t_2$ . For  $\mu\nu < 0$ ,  $t_2^2 + \mu\nu = 0$  yields another boundary for the zero edge states determined from band touching EPs. Two topological zero edge states exist in the regions  $\gamma^2 - t_2^2 < t_1^2 < \gamma^2 + t_2^2$  for one intercell coupling  $t_2$  vanishing under OBC [168].

*Topological edge states.*—The bulk topology relates to the (dis)appearance of edge states at the interfaces where topological invariant ( $w$ ) changes. We consider systems with complete unit cells ( $N = 4n$ ) with one  $t_2$  vanishes (see Supplemental Material G for the case with a defective unit cell [135]). In system  $b$ , two edge states localize on the left and right boundaries, respectively in all blue regions of Fig. 3(c). In system  $a$ , this occurs only in region V; and both two edge states localize on the right (left) boundary in regions I and III (II and IV).

For system  $b$ , the left edge state is  $\psi_{2j} = 0$  and

$$\psi_{2j+1} = -[(\mu + \nu) + (-1)^j (\mu - \nu)] / (2t_2) \psi_{2j-1}, \quad (8)$$

at  $N \gg 1$ . The right edge state is a left-right spatial reflection of the left edge state [Fig. 3(d)]. Anomalous edge states localize in one unit cell at system boundary at the EPs ( $t_1^2 = \gamma^2$ ) [107, 119, 120]. At  $t_1 = -\gamma$ , the left (right) edge state is  $\psi_1 = 1$  ( $\psi_N = 1$ ); at  $t_1 = \gamma$ , the left edge state is  $\psi_1 = -(+)\psi_3 = 1$  and the right edge state is  $\psi_N = -(+)\psi_{N-2} = 1$  when  $t_1/t_2 > 0$  ( $t_1/t_2 < 0$ ).

In contrast, for system  $a$ , the left edge state is  $\psi_{2j} = 0$  and  $\psi_{2j+1} = (-\nu/t_2) \psi_{2j-1}$ ; the right edge state is  $\psi_{2j-1} = 0$  and  $\psi_{N-2j} = (-\mu/t_2) \psi_{N+2-2j}$  with a different decay rate  $-\mu/t_2$  [Fig. 3(d)]. The imaginary gauge field induces imbalanced probability distributions between edge states. The green (red) ribbon in Fig. 3(c) indicates  $|\mu/t_2| < 1$  ( $|\nu/t_2| < 1$ ), both edge states localize on the right (left) boundary. The edge states are  $\psi_1 = 1$  ( $\psi_N = 1$ ) for  $t_1/t_2 < 0$  ( $t_1/t_2 > 0$ ) at the EPs.

*Discussion and Conclusion.*—Figure 4(a) depicts the chiral-inversion symmetric non-Hermitian SSH model of system  $b$  with staggered gain and loss  $\Gamma$ , where chiral symmetry and inversion symmetry are not separately hold. System shown in Fig. 4(a) is equivalent to the chiral-inversion symmetric non-Hermitian Creutz ladder [Fig. 4(b)]. The Creutz ladder has a  $\pi$  magnetic flux in each plaquette [169]. The Creutz ladder in Refs. [119–121] is equivalent to system  $a$  through a similar transformation  $U = I_{2n} \otimes (i\sigma_x + I_2)$  (see Supplemental Material H [135]), where bulk-boundary correspondence fails because gain and loss associated with real magnetic flux breaks chiral-inversion symmetry and effectively creates imaginary magnetic flux under PBC.

Time-reversal (Inversion) symmetry prevents nonzero real (imaginary) magnetic flux. An attenuation (amplification) factor  $e^{-\phi}$  accompanied with the corresponding amplification (attenuation) factor  $e^{\phi}$  in the direction concerned can prevent nonzero imaginary magnetic

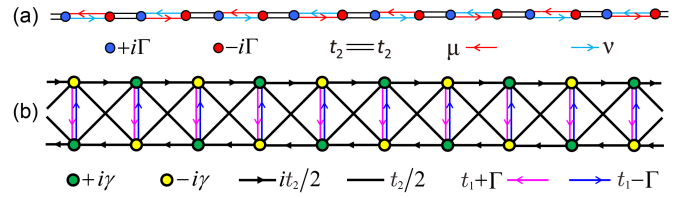


FIG. 4. Chiral-inversion symmetric (a) non-Hermitian SSH model of system  $b$  in Fig. 1 ( $H_b$ ) with staggered gain and loss  $\Gamma$ , (b) non-Hermitian Creutz ladder that equivalent to (a).

flux. This is enabled under inversion symmetry ( $\mathcal{P}$ ) or combined inversion symmetries such as chiral-inversion ( $\mathcal{SP}$ ) symmetry, charge-conjugation inversion ( $\mathcal{CP}$ ) symmetry, and parity-time ( $\mathcal{PT}$ ) symmetry. For a 2D non-Hermitian Chern insulator ( $m + t \cos k_x + t \cos k_y$ )  $\sigma_x + (t \sin k_x + i\gamma) \sigma_y + t \sin k_y \sigma_z$  [130], we write its energy bands as  $\pm \sqrt{\mu\nu + t^2 + t^2 \sin^2 k_y} + 2t\sqrt{\mu\nu} \cos(k_x + i\phi)$ , where we set  $\mu = m + t \cos k_y + \gamma$ ,  $\nu = m + t \cos k_y - \gamma$ , and  $\sqrt{\mu/\nu} = e^{-\phi}$  (for  $\mu\nu > 0$ ). An imaginary magnetic flux exists in the  $x$  direction, but not in the  $y$  direction; considerable difference between PBC and OBC spectra is observed in the  $x$  direction [130]. Introducing the non-Hermiticity under inversion symmetry prevents nonzero imaginary magnetic flux under PBC because of the cancellation between amplification and attenuation factors  $e^{\pm\phi}$  in the  $x$  direction and enables the bulk-boundary correspondence. By applying the same procedure done for the non-Hermitian SSH model of system  $b$ , we can obtain an equivalent bulk Bloch Hamiltonian  $h_{b,CI}(k_x, k_y) = (\sqrt{\mu\nu} + t \cos k_x) \sigma_x + (t \sin k_x) \sigma_y + (t \sin k_y) \sigma_z$  after removing the imaginary gauge field (see Supplemental Material I [135]). The energy bands are  $\pm \sqrt{\mu\nu + t^2 + t^2 \sin^2 k_y} + 2t\sqrt{\mu\nu} \cos k_x$ . The bulk topology of  $h_{b,CI}(k_x, k_y)$  correctly predicts the topological phase transition and the (non)existence of edge states for the Chern insulator under OBC.

Bulk-boundary correspondence fails for nonzero imaginary magnetic flux under PBC if the flux vanishes under OBC; the bulk-boundary correspondence recovers by alternatively introducing non-Hermiticity under symmetry, which prevents nonzero imaginary magnetic flux; and topological invariant can be constructed from the bulk Bloch Hamiltonian. The non-Bloch topological invariant and exotic bulk-boundary correspondence [123, 124] are elaborated from the viewpoint of (conventional) bulk-boundary correspondence. Our findings provide new insights from non-Hermitian AB effect and shed light on non-Hermitian topological phases of matter.

We acknowledge the support of NSFC (Grant Nos. 11605094 and 11874225).

- 
- \* jinliang@nankai.edu.cn
- [1] A. Y. Kitaev, Unpaired Majorana fermions in quantum wires, *Phys. Usp.* **44**, 131 (2001).
  - [2] S. Ryu and Y. Hatsugai, Topological Origin of Zero-Energy Edge States in Particle-Hole Symmetric Systems, *Phys. Rev. Lett.* **89**, 077002 (2002).
  - [3] M. Greiner, O. Mandel, T. Esslinger, T. W. Hänsch, and I. Bloch, Quantum phase transition from a superfluid to a Mott insulator in a gas of ultracold atoms. *Nature* **415**, 39 (2002).
  - [4] S. Murakami, N. Nagaosa, and S.-C. Zhang, Spin-Hall Insulator, *Phys. Rev. Lett.* **93**, 156804 (2004).
  - [5] C. L. Kane and E. J. Mele, Quantum Spin Hall Effect in Graphene, *Phys. Rev. Lett.* **95**, 226801 (2005).
  - [6] B. A. Bernevig, T. L. Hughes, and S. C. Zhang, Quantum spin Hall effect and topological phase transition in HgTe quantum wells, *Science* **314**, 1757 (2006).
  - [7] L. Fu and C. L. Kane, Topological insulators with inversion symmetry, *Phys. Rev. B* **76**, 045302 (2007).
  - [8] L. Fu, C. Kane, and E. Mele, Topological Insulators in Three Dimensions, *Phys. Rev. Lett.* **98**, 106803 (2007).
  - [9] A. P. Schnyder, S. Ryu, A. Furusaki, and A. W. W. Ludwig, Classification of topological insulators and superconductors in three spatial dimensions, *Phys. Rev. B* **78**, 195125 (2008).
  - [10] H. Zhang, C.-X. Liu, X.-L. Qi, X. Dai, Z. Fang, S.-C. Zhang, Topological Insulators in the Bi<sub>2</sub>Se<sub>3</sub>, Bi<sub>2</sub>Te<sub>3</sub> and Sb<sub>2</sub>Te<sub>3</sub> with a single Dirac cone on the surface, *Nat. Phys.* **5**, 438 (2009).
  - [11] S. Ryu, A. P. Schnyder, A. Furusaki, and A. W. W. Ludwig, Topological insulators and superconductors: tenfold way and dimensional hierarchy, *New J. Phys.* **12**, 065010 (2010).
  - [12] M. Z. Hasan and C. L. Kane, Colloquium: Topological insulators, *Rev. Mod. Phys.* **82**, 3045 (2010).
  - [13] G. Xu, H. Weng, Z. Wang, X. Dai, and Z. Fang, Chern Semimetal and the Quantized Anomalous Hall Effect in HgCr<sub>2</sub>Se<sub>4</sub>, *Phys. Rev. Lett.* **107**, 186806 (2011).
  - [14] A. A. Burkov and L. Balents, Weyl semimetal in a topological insulator multilayer, *Phys. Rev. Lett.* **107**, 127205 (2011).
  - [15] X.-L. Qi and S.-C. Zhang, Topological insulators and superconductors, *Rev. Mod. Phys.* **83**, 1057 (2011).
  - [16] S. M. Young, S. Zaheer, J. C. Y. Teo, C. L. Kane, E. J. Mele, and A. M. Rappe, Dirac Semimetal in Three Dimensions, *Phys. Rev. Lett.* **108**, 140405 (2012).
  - [17] Z. Wang, Y. Sun, X.-Q. Chen, C. Franchini, G. Xu, H. Weng, X. Dai, and Z. Fang, Dirac semimetal and topological phase transitions in A<sub>3</sub>Bi (A=Na, K, Rb), *Phys. Rev. B* **85**, 195320 (2012).
  - [18] C.-E. Bardyn, M. A. Baranov, E. Rico, A. İmamoğlu, P. Zoller, and S. Diehl, Majorana modes in driven-dissipative atomic superfluids with a zero Chern number, *Phys. Rev. Lett.* **109**, 130402 (2012).
  - [19] L. Tarruell, D. Greif, T. Uehlinger, G. Jotzu, and T. Esslinger, Creating, moving and merging Dirac points with a Fermi gas in a tunable honeycomb lattice, *Nature* **483**, 302 (2012).
  - [20] Z. Liu, D. L. Kovrizhin, and E. J. Bergholtz, Bulk-edge correspondence in fractional Chern insulators, *Phys. Rev. B* **88**, 081106(R) (2013).
  - [21] Z. Wang, H. Weng, Q. Wu, X. Dai, and Z. Fang, Three-dimensional Dirac semimetal and quantum transport in Cd<sub>3</sub>As<sub>2</sub>, *Phys. Rev. B* **88**, 125427 (2013).
  - [22] X.-J. Liu, K. T. Law, T. K. Ng, and P. A. Lee, Detecting Topological Phases in Cold Atoms, *Phys. Rev. Lett.* **111**, 120402 (2013).
  - [23] D.-L. Deng, S.-T. Wang, and L.-M. Duan, Direct probe of topological order for cold atoms, *Phys. Rev. A* **90**, 041601(R) (2014).
  - [24] Z. K. Liu, B. Zhou, Y. Zhang, Z. J. Wang, H. M. Weng, D. Prabhakaran, S.-K. Mo, Z. X. Shen, Z. Fang, X. Dai, Z. Hussain, and Y. L. Chen, Discovery of a Three-Dimensional Topological Dirac Semimetal, Na<sub>3</sub>Bi, *Science* **343**, 864 (2014).
  - [25] M. Xiao, G. Ma, Z. Yang, P. Sheng, Z. Q. Zhang, and C. T. Chan, Geometric phase and band inversion in periodic acoustic systems, *Nat. Phys.* **11**, 240 (2015).
  - [26] H. Weng, C. Fang, Z. Fang, B. A. Bernevig, and X. Dai, Weyl Semimetal Phase in Noncentrosymmetric Transition-Metal Monophosphides, *Phys. Rev. X* **5**, 011029 (2015).
  - [27] L. Lu, Z. Wang, D. Ye, L. Ran, L. Fu, J. D. Joannopoulos, and M. Soljačić, Experimental observation of Weyl points, *Science*, **349**, 622 (2015).
  - [28] D. Leykam, M. C. Rechtsman, and Y. D. Chong, Anomalous Topological Phases and Unpaired Dirac Cones in Photonic Floquet Topological Insulators, *Phys. Rev. Lett.* **117**, 013902 (2016).
  - [29] C.-K. Chiu, J. C. Y. Teo, A. P. Schnyder, and S. Ryu, Classification of topological quantum matter with symmetries, *Rev. Mod. Phys.* **88**, 035005 (2016).
  - [30] F. K. Kunst, M. Trescher, and E. J. Bergholtz, Anatomy of topological surface states: Exact solutions from destructive interference on frustrated lattices, *Phys. Rev. B* **96**, 085443 (2017).
  - [31] F. K. Kunst, G. van Miert, and E. J. Bergholtz, Lattice models with exactly solvable topological hinge and corner states, *Phys. Rev. B* **97**, 241405 (2018).
  - [32] N. P. Armitage, E. J. Mele, and A. Vishwanath, Weyl and Dirac semimetals in three-dimensional solids, *Rev. Mod. Phys.* **90**, 015001 (2018).
  - [33] M. Atala, M. Aidelsburger, J. T. Barreiro, D. Abanin, Takuya Kitagawa, E. Demler, and I. Bloch, Direct measurement of the Zak phase in topological Bloch bands, *Nat. Phys.* **9**, 795 (2013).
  - [34] L. Lu, J. D. Joannopoulos, and M. Soljačić, Topological photonics, *Nat. Photon.* **8**, 821 (2014).
  - [35] S. Mittal, S. Ganeshan, J. Fan, A. Vaez, and M. Hafezi, Measurement of topological invariants in a 2D photonic system, *Nat. Photon.* **10**, 180 (2016).
  - [36] Q. Lin, M. Xiao, L. Yuan, and S. Fan, Photonic Weyl point in a two-dimensional resonator lattice with a synthetic frequency dimension, *Nat. Commun.* **7**, 13731 (2016).
  - [37] M. Hafezi, E. A. Demler, M. D. Lukin, and J. M. Taylor, Robust optical delay lines with topological protection, *Nat. Phys.* **7**, 907 (2011).
  - [38] M. Aidelsburger, M. Atala, M. Lohse, J. T. Barreiro, B. Paredes, and I. Bloch, Realization of the Hofstadter Hamiltonian with Ultracold Atoms in Optical Lattices, *Phys. Rev. Lett.* **111**, 185301 (2013).
  - [39] N. Goldman, J. C. Budich, and P. Zoller, Topological quantum matter with ultracold gases in optical lattices, *Nat. Phys.* **12**, 639 (2016).



- [40] T. Ozawa, H. M. Price, A. Amo, N. Goldman, M. Hafezi, L. Lu, M. C. Rechtsman, D. Schuster, J. Simon, O. Zilberberg, and I. Carusotto, Topological photonics, arXiv: 1802.04173.
- [41] N. R. Cooper, J. Dalibard, and I. B. Spielman, Topological bands for ultracold atoms, arXiv: 1803.00249.
- [42] C. M. Bender and S. Boettcher, Real Spectra in Non-Hermitian Hamiltonians Having  $\mathcal{PT}$  Symmetry, Phys. Rev. Lett. **80**, 5243 (1998).
- [43] A. Mostafazadeh, Pseudo-Hermiticity versus  $\mathcal{PT}$  symmetry: The necessary condition for the reality of the spectrum of a non-Hermitian Hamiltonian, J. Math. Phys. **43**, 205 (2002).
- [44] C. M. Bender, Making sense of non-Hermitian Hamiltonians, Rep. Prog. Phys. **70**, 947 (2007).
- [45] K. G. Makris, R. El-Ganainy, D. N. Christodoulides, and Z. H. Musslimani, Beam Dynamics in  $\mathcal{PT}$  Symmetric Optical Lattices, Phys. Rev. Lett. **100**, 103904 (2008).
- [46] S. Klaiman, U. Günther, and N. Moiseyev, Visualization of Branch Points in  $\mathcal{PT}$ -Symmetric Waveguides, Phys. Rev. Lett. **101**, 080402 (2008).
- [47] Z. H. Musslimani, K. G. Makris, R. El-Ganainy, and D. N. Christodoulides, Optical Solitons in  $\mathcal{PT}$  Periodic Potentials, Phys. Rev. Lett. **100**, 030402 (2008).
- [48] I. Rotter, A non-Hermitian Hamilton operator and the physics of open quantum systems, J. Phys. A **42**, 153001 (2009).
- [49] A. Guo, G. J. Salamo, D. Duchesne, R. Morandotti, M. Volatier-Ravat, V. Aimez, G. A. Siviloglou, and D. N. Christodoulides,  $\mathcal{PT}$ -Symmetry Breaking and Laser-Absorber Modes in Optical Scattering Systems, Phys. Rev. Lett. **103**, 093902 (2009).
- [50] C. E. Rüter, K. G. Makris, R. El-Ganainy, D. N. Christodoulides, M. Segev, and D. Kip, Observation of parity-time symmetry in optics, Nat. Phys. **6**, 192 (2010).
- [51] Y. D. Chong, L. Ge, H. Cao, and A. D. Stone, Coherent Perfect Absorbers: Time-Reversed Lasers, Phys. Rev. Lett. **105**, 053901 (2010).
- [52] N. Moiseyev, *Non-Hermitian Quantum Mechanics* (Cambridge Univ. Press, 2011).
- [53] M. Liertzer, L. Ge, A. Cerjan, A. D. Stone, H. E. Türeci, and S. Rotter, Pump-Induced Exceptional Points in Lasers, Phys. Rev. Lett. **108**, 173901 (2012).
- [54] A. Regensburger, M.-A. Miri, C. Bersch, J. Näger, G. Onishchukov, D. N. Christodoulides, and Ulf Peschel, Observation of Defect States in  $\mathcal{PT}$ -Symmetric Optical Lattices, Phys. Rev. Lett. **110**, 223902 (2013).
- [55] B. Peng, S. K. Ozdemir, F. Lei, F. Monifi, M. Gianfreda, G. L. Long, S. Fan, F. Nori, C. M. Bender, and L. Yang, Parity-time-symmetric whispering-gallery microcavities, Nat. Phys. **10**, 394 (2014).
- [56] L. Chang, X. Jiang, S. Hua, C. Yang, J. Wen, L. Jiang, G. Li, G. Wang, and M. Xiao, Parity-time symmetry and variable optical isolation in active-passive-coupled microresonators, Nat. Photon. **8**, 524 (2014).
- [57] L. Feng, Z. J. Wong, R.-M. Ma, Y. Wang, and X. Zhang, Single-mode laser by parity-time symmetry breaking, Science **346**, 972 (2014).
- [58] H. Hodaei, M.-A. Miri, M. Heinrich, D. N. Christodoulides, and M. Khajavikhan, Parity-time-symmetric microring lasers, Science **346**, 975 (2014).
- [59] R. Fleury, D. Sounas, and A. Alù, An invisible acoustic sensor based on parity-time symmetry, Nat. Commun. **6**, 5905 (2015).
- [60] H. Cao and J. Wiersig, Dielectric microcavities: Model systems for wave chaos and non-Hermitian physics, Rev. Mod. Phys. **87**, 61 (2015).
- [61] F. Monticone, C. A. Valagiannopoulos, and A. Alù, Parity-Time Symmetric Nonlocal Metasurfaces: All-Angle Negative Refraction and Volumetric Imaging, Phys. Rev. X **6**, 041018 (2016).
- [62] K. Ding, G. Ma, M. Xiao, Z. Q. Zhang, and C. T. Chan, Emergence, Coalescence, and Topological Properties of Multiple Exceptional Points and Their Experimental Realization, Phys. Rev. X **6**, 021007 (2016).
- [63] A. Cerjan, A. Raman, and S. Fan, Exceptional Contours and Band Structure Design in Parity-Time Symmetric Photonic Crystals, Phys. Rev. Lett. **116**, 203902 (2016).
- [64] Z. Zhang, Y. Zhang, J. Sheng, L. Yang, M.-A. Miri, D. N. Christodoulides, B. He, Y. Zhang, and M. Xiao, Observation of Parity-Time Symmetry in Optically Induced Atomic Lattices, Phys. Rev. Lett. **117**, 123601 (2016).
- [65] L. Ge, Symmetry-protected zero-mode laser with a tunable spatial profile, Phys. Rev. A **95**, 023812 (2017).
- [66] W. Chen, S. K. Ozdemir, G. Zhao, J. Wiersig, and L. Yang, Exceptional points enhance sensing in an optical microcavity, Nature **548**, 192 (2017).
- [67] H. Hodaei, A. U. Hassan, S. Wittek, H. Garcia-Gracia, R. El-Ganainy, D. N. Christodoulides, and M. Khajavikhan, Enhanced sensitivity at higher-order exceptional points, Nature **548**, 187 (2017).
- [68] K. Kawabata, Y. Ashida, and M. Ueda, Information Retrieval and Criticality in Parity-Time-Symmetric Systems, Phys. Rev. Lett. **119**, 190401 (2017).
- [69] Y. Ashida, S. Furukawa, and M. Ueda, Parity-time-symmetric quantum critical phenomena, Nat. Commun. **8**, 15791 (2017).
- [70] S. Assaworarith, X. Yu, and S. Fan, Robust wireless power transfer using a nonlinear parity-time-symmetric circuit, Nature, **546**, 387 (2017).
- [71] H. Zhou, C. Peng, Y. Yoon, C. W. Hsu, K. A. Nelson, L. Fu, J. D. Joannopoulos, M. Soljačić, and B. Zhen, Observation of bulk Fermi arc and polarization half charge from paired exceptional points, Science **359**, 1009 (2018).
- [72] G. Harari, M. A. Bandres, Y. Lumer, M. C. Rechtsman, Y. D. Chong, M. Khajavikhan, D. N. Christodoulides, and M. Segev, Topological insulator laser: Theory, Science **359**, eaar4003 (2018).
- [73] M. A. Bandres, S. Wittek, G. Harari, M. Parto, J. Ren, M. Segev, D. Christodoulides, and M. Khajavikhan, Topological insulator laser: Experiments, Science **359**, eaar4005 (2018).
- [74] L. Feng, R. El-Ganainy, and L. Ge, Non-Hermitian photonics based on parity-time symmetry, Nat. Photon. **11**, 752 (2017).
- [75] R. El-Ganainy, K. G. Makris, M. Khajavikhan, Z. H. Musslimani, S. Rotter, and D. N. Christodoulides, Nat. Phys. **14**, 11 (2018).
- [76] S. Diehl, E. Rico, M. A. Baranov, and P. Zoller, Topology by dissipation in atomic quantum wires, Nat. Phys. **7**, 971 (2011).
- [77] Y. C. Hu and T. L. Hughes, Absence of topological insulator phases in non-Hermitian  $\mathcal{PT}$ -symmetric Hamiltonians, Phys. Rev. B **84**, 153101 (2011).

- [78] K. Esaki, M. Sato, K. Hasebe, and M. Kohmoto, Edge states and topological phases in non-Hermitian systems, *Phys. Rev. B* **84**, 205128 (2011).
- [79] G. Q. Liang and Y. D. Chong, Optical Resonator Analog of a Two-Dimensional Topological Insulator, *Phys. Rev. Lett.* **110**, 203904 (2013).
- [80] B. Zhu, R. Lü, and S. Chen, PT symmetry in the non-Hermitian Su-Schrieffer-Heeger model with complex boundary potentials, *Phys. Rev. A* **89**, 062102 (2014).
- [81] C. Yuce, Topological phase in a non-Hermitian PT symmetric system, *Phys. Lett. A* **379**, 1213 (2015).
- [82] X. Wang, T. Liu, Y. Xiong, and P. Tong, Spontaneous PT-symmetry breaking in non-Hermitian Kitaev and extended Kitaev models, *Phys. Rev. A* **92**, 012116 (2015).
- [83] H. Zhao, S. Longhi, and L. Feng, Robust Light State by Quantum Phase Transition in Non-Hermitian Optical Materials, *Sci. Rep.* **5**, 17022 (2015).
- [84] S. Malzard, C. Poli, and H. Schomerus, Topologically Protected Defect States in Open Photonic Systems with Non-Hermitian Charge-Conjugation and Parity-Time Symmetry, *Phys. Rev. Lett.* **115**, 200402 (2015).
- [85] M. S. Rudner and L. S. Levitov, Topological Transition in a Non-Hermitian Quantum Walk, *Phys. Rev. Lett.* **102**, 065703 (2009).
- [86] H. Schomerus, Topologically protected midgap states in complex photonic lattices, *Opt. Lett.* **38**, 1912 (2013).
- [87] C. Poli, M. Bellec, U. Kuhl, F. Mortessagne, and H. Schomerus, Selective enhancement of topologically induced interface states in a dielectric resonator chain, *Nat. Commun.* **6**, 6710 (2015).
- [88] J. M. Zeuner, M. C. Rechtsman, Y. Plotnik, Y. Lumer, S. Nolte, M. S. Rudner, M. Segev, and A. Szameit, Observation of a Topological Transition in the Bulk of a Non-Hermitian System, *Phys. Rev. Lett.* **115**, 040402 (2015).
- [89] S. Weimann, M. Kremer, Y. Plotnik, Y. Lumer, S. Nolte, K. G. Makris, M. Segev, M. C. Rechtsman, and A. Szameit, Topologically protected bound states in photonic parity-time-symmetric crystals, *Nat. Mater.* **16**, 433 (2017).
- [90] H. Zhao, P. Miao, M. H. Teimourpour, S. Malzard, R. El-Ganainy, H. Schomerus, and L. Feng, Topological hybrid silicon microlasers, *Nat. Commun.* **9**, 981 (2018).
- [91] M. Pan, H. Zhao, P. Miao, S. Longhi, and L. Feng, Photonic zero mode in a non-Hermitian photonic lattice, *Nat. Commun.* **9**, 1308 (2018).
- [92] M. Pardo, S. Wittek, H. Hodaei, G. Harari, M. A. Bandres, J. Ren, M. C. Rechtsman, M. Segev, D. N. Christodoulides, and M. Khajavikhan, Edge-Mode Lasing in 1D Topological Active Arrays, *Phys. Rev. Lett.* **120**, 113901 (2018).
- [93] S. Lieu, Topological phases in the non-Hermitian Su-Schrieffer-Heeger model, *Phys. Rev. B* **97**, 045106 (2018).
- [94] R. Wang, X. Z. Zhang, and Z. Song, Dynamical topological invariant for non-Hermitian Rice-Mele model, *Phys. Rev. A* **98**, 042120 (2018).
- [95] K. Kawabata, Y. Ashida, H. Katsura, and M. Ueda, Parity-time-symmetric topological superconductor, *Phys. Rev. B* **98**, 085116 (2018).
- [96] K. Kawabata, S. Higashikawa, Z. Gong, Y. Ashida, and M. Ueda, Topological unification of time-reversal and particle-hole symmetries in non-Hermitian physics, arXiv:1804.04676.
- [97] L. J. Lang, Y. Wang, H. Wang, and Y. D. Chong, Effects of Non-Hermiticity on Su-Schrieffer-Heeger Defect States, *Phys. Rev. B* **98**, 094307 (2018).
- [98] C. A. Downing and G. Weick, Topological collective plasmons in bipartite chains of metallic nanoparticles, *Phys. Rev. B* **95**, 125426 (2017).
- [99] L. Jin, P. Wang, and Z. Song, Su-Schrieffer-Heeger chain with one pair of PT-symmetric defects, *Sci. Rep.* **7**, 5903 (2017).
- [100] M. Klett, H. Cartarius, D. Dast, J. Main, and G. Wunner, Relation between PT-symmetry breaking and topologically nontrivial phases in the Su-Schrieffer-Heeger and Kitaev models, *Phys. Rev. A* **95**, 053626 (2017).
- [101] H. Menke and M. M. Hirschmann, Topological quantum wires with balanced gain and loss, *Phys. Rev. B* **95**, 174506 (2017).
- [102] L. Jin, Topological phases and edge states in a non-Hermitian trimerized optical lattice, *Phys. Rev. A* **96**, 032103 (2017).
- [103] W. Hu, H. Wang, P. P. Shum, and Y. D. Chong, Exceptional points in a non-Hermitian topological pump, *Phys. Rev. B* **95**, 184306 (2017).
- [104] J. González and R. A. Molina, Topological protection from exceptional points in Weyl and nodal-line semimetals, *Phys. Rev. B* **96**, 045437 (2017).
- [105] L. Xiao, X. Zhan, Z. H. Bian, K. K. Wang, X. Zhang, X. P. Wang, J. Li, K. Mochizuki, D. Kim, N. Kawakami, W. Yi, H. Obuse, B. C. Sanders, and P. Xue, Observation of topological edge states in parity-time-symmetric quantum walks, *Nat. Phys.* **13**, 1117 (2017).
- [106] W. Zhu, X. Fang, D. Li, Y. Sun, Y. Li, Y. Jing, and H. Chen, Simultaneous Observation of a Topological Edge State and Exceptional Point in an Open and Non-Hermitian Acoustic System, *Phys. Rev. Lett.* **121**, 124501 (2018).
- [107] D. Leykam, K. Y. Bliokh, C. Huang, Y. D. Chong, and F. Nori, Edge Modes, Degeneracies, and Topological Numbers in Non-Hermitian Systems, *Phys. Rev. Lett.* **118**, 040401 (2017).
- [108] Y. Xu, S.-T. Wang, and L.-M. Duan, Weyl Exceptional Rings in a Three-Dimensional Dissipative Cold Atomic Gas, *Phys. Rev. Lett.* **118**, 045701 (2017).
- [109] H. Shen, B. Zhen, and L. Fu, Topological Band Theory for Non-Hermitian Hamiltonians, *Phys. Rev. Lett.* **120**, 146402 (2018).
- [110] A. Y. Song, P. B. Catrysse, and S. Fan, Broadband Control of Topological Nodes in Electromagnetic Fields, *Phys. Rev. Lett.* **120**, 193903 (2018).
- [111] C. Yuce, Edge states at the interface of non-Hermitian systems, *Phys. Rev. A* **97**, 042118 (2018).
- [112] C. Yin, H. Jiang, L. Li, R. Lü, and S. Chen, Geometrical meaning of winding number and its characterization of topological phases in one-dimensional chiral non-Hermitian systems, *Phys. Rev. A* **97**, 052115 (2018).
- [113] H. Shen and L. Fu, Quantum Oscillation from In-Gap States and a Non-Hermitian Landau Level Problem, *Phys. Rev. Lett.* **121**, 026403 (2018).
- [114] S. Lieu, Topological symmetry classes for non-Hermitian models and connections to the bosonic Bogoliubov-de Gennes equation, *Phys. Rev. B* **98**, 115135 (2018).
- [115] H. Jiang, C. Yang, and S. Chen, Topological invariants,

- phase diagrams and discrepancy for non-Hermitian systems without chiral symmetry, *Phys. Rev. A* **98**, 052116 (2018).
- [116] S. Malzard and H. Schomerus, Bulk and edge-state arcs in non-Hermitian coupled-resonator arrays, arXiv:1805.08161.
- [117] M. Klett, H. Cartarius, D. Dast, J. Main, and G. Wunner, Topological edge states in the Su-Schrieffer-Heeger model subject to balanced particle gain and loss, arXiv:1802.06128.
- [118] In this work, the word “bulk-boundary correspondence” refers to the conventional bulk-boundary correspondence.
- [119] V. M. Martinez Alvarez, J. E. Barrios Vargas, and L. E. F. Foa Torres, Non-Hermitian robust edge states in one dimension: Anomalous localization and eigenspace condensation at exceptional points, *Phys. Rev. B* **97**, 121401(R) (2018).
- [120] T. E. Lee, Anomalous Edge State in a Non-Hermitian Lattice, *Phys. Rev. Lett.* **116**, 133903 (2016).
- [121] Y. Xiong, Why does bulk boundary correspondence fail in some non-hermitian topological models, *J. Phys. Commun.* **2**, 035043 (2018).
- [122] F. K. Kunst, E. Edvardsson, J. C. Budich, and E. J. Bergholtz, Biorthogonal Bulk-Boundary Correspondence in Non-Hermitian Systems, *Phys. Rev. Lett.* **121**, 026808 (2018).
- [123] S. Yao and Z. Wang, Edge States and Topological Invariants of Non-Hermitian Systems, *Phys. Rev. Lett.* **121**, 086803 (2018).
- [124] Z. Gong, Y. Ashida, K. Kawabata, K. Takasan, S. Higashikawa, and M. Ueda, Topological phases of non-Hermitian systems, *Phys. Rev. X* **8**, 031079 (2018).
- [125] C. H. Lee and R. Thomale, Anatomy of skin modes and topology in non-Hermitian systems, arXiv:1809.02125.
- [126] Z. Yang and J. Hu, Nodal Line Semimetals under non-Hermitian Perturbations—Emerging Hopf-Link Exceptional Line Semimetals, arXiv:1807.05661.
- [127] H. Wang, J. Ruan, and H. Zhang, Non-Hermitian nodal-line semimetals, arXiv:1808.06162.
- [128] V. M. Martinez Alvarez, J. E. Barrios Vargas, M. Berdakin, and L. E. F. Foa Torres, Topological states of non-Hermitian systems, *Eur. Phys. J. Special Topics*, **1** (2018).
- [129] S. Yao, F. Song, and Z. Wang, Non-Hermitian Chern bands, *Phys. Rev. Lett.* **121**, 136802 (2018).
- [130] K. Kawabata, K. Shiozaki, and M. Ueda, Anomalous helical edge states in a non-Hermitian Chern insulator, *Phys. Rev. B* **98**, 165148 (2018).
- [131] W. P. Su, J. R. Schrieffer, and A. J. Heeger, Solitons in polyacetylene, *Phys. Rev. Lett.* **42**, 1698 (1979).
- [132] N. Hatano and D. R. Nelson, Localization Transitions in Non-Hermitian Quantum Mechanics, *Phys. Rev. Lett.* **77**, 570 (1996).
- [133] S. Longhi, D. Gatti, and G. Della Valle, Non-Hermitian transparency and one-way transport in low-dimensional lattices by an imaginary gauge field, *Phys. Rev. B* **92**, 094204 (2015).
- [134] B. Midya, H. Zhao, and L. Feng, Non-Hermitian photonics promises exceptional topology of light, *Nat. Commun.* **9**, 2674 (2018).
- [135] See online Supplemental Material for more details on the imaginary gauge field and non-Hermitian AB effect, the bulk state inverse participation ratio, the proof of identical energy spectra of systems  $a$  and  $b$  under OBC, the chiral-inversion symmetric systems, the topological characterization, the finite effect on energy spectra, the edge states for system with a defective unit cell, the equivalence between non-Hermitian SSH models and Creutz ladders, and the 2D non-Hermitian topological systems.
- [136] X. Z. Zhang, Z. Song, Momentum-independent reflectionless transmission in the non-Hermitian time-reversal symmetric system, *Ann. Phys. (N.Y.)* **339**, 109 (2013).
- [137] K. Fang, Z. Yu, and S. Fan, Photonic Aharonov-Bohm Effect Based on Dynamic Modulation, *Phys. Rev. Lett.* **108**, 153901 (2012).
- [138] K. Fang, Z. Yu, and S. Fan, Realizing effective magnetic field for photons by controlling the phase of dynamic modulation, *Nat. Photon.* **6**, 782 (2012).
- [139] E. Li, B. J. Eggleton, K. Fang, and S. Fan, Photonic Aharonov-Bohm effect in photon-phonon interactions, *Nature Commun* **5**, 3225 (2014).
- [140] M. Hafezi, Measuring Topological Invariants in Photonic Systems, *Phys. Rev. Lett.* **112**, 210405 (2014).
- [141] L. Jin and Z. Song, Parity-time symmetry under magnetic flux, *Phys. Rev. A* **93**, 062110 (2016).
- [142] L. Jin, P. Wang, and Z. Song, One-way light transport controlled by synthetic magnetic fluxes and PT-symmetric resonators, *New J. Phys.* **19**, 015010 (2017).
- [143] L. Jin, Parity-time-symmetric coupled asymmetric dimers, *Phys. Rev. A* **97**, 012121 (2018).
- [144] Peierls phase factor refers  $e^{\pm i\Phi}$  [39], where  $\Phi$  is imaginary  $\Phi = i\phi$  for the asymmetric coupling  $\sqrt{\mu\nu}e^{\mp\phi}$ .
- [145] W. D. Heiss and H. L. Harney, The chirality of exceptional points, *Eur. Phys. J. D* **17**, 149 (2001).
- [146] C. Dembowski, H.-D. Gräf, H. L. Harney, A. Heine, W. D. Heiss, H. Rehfeld, and A. Richter, Experimental Observation of the Topological Structure of Exceptional Points, *Phys. Rev. Lett.* **86**, 787 (2001).
- [147] M. V. Berry, *Czech. J. Phys.* **54**, 1039 (2004).
- [148] A. A. Mailybaev, O. N. Kirillov, and A. P. Seyranian, Geometric phase around exceptional points, *Phys. Rev. A* **72**, 014104 (2005).
- [149] M. Müller and I. Rotter, Exceptional points in open quantum systems, *J. Phys. A: Math. Theor.* **41**, 244018 (2008).
- [150] R. Uzdin, A. Mailybaev, and N. Moiseyev, On the observability and asymmetry of adiabatic state flips generated by exceptional points, *J. Phys. A* **44**, 435302 (2011).
- [151] W. D. Heiss, The physics of exceptional points, *J. Phys. A* **45**, 444016 (2012).
- [152] S.-D. Liang and G.-Y. Huang, Topological invariance and global Berry phase in non-Hermitian systems, *Phys. Rev. A* **87**, 012118 (2013).
- [153] B. Zhen, C. W. Hsu, Y. Igarashi, L. Lu, I. Kaminer, A. Pick, S.-L. Chua, J. D. Joannopoulos, and M. Soljačić, *Nature* **525**, 354 (2015).
- [154] J. Doppler, A. A. Mailybaev, J. Böhm, U. Kuhl, A. Girschik, F. Libisch, T. J. Milburn, P. Rabl, N. Moiseyev, and S. Rotter, Dynamically encircling an exceptional point for asymmetric mode switching, *Nature* **537**, 76 (2016).
- [155] H. Xu, D. Mason, L. Jiang, and J. G. E. Harris, Topological energy transfer in an optomechanical system with exceptional points, *Nature* **537**, 80 (2016).
- [156] D. Heiss, Circling exceptional points, *Nat. Phys.* **12**, 823



- (2016).
- [157] A. U. Hassan, B. Zhen, M. Soljačić, M. Khajavikhan, and D. N. Christodoulides, Phys. Rev. Lett. **118**, 093002 (2017).
  - [158] T. Goldzak, A. A. Mailybaev, and Nimrod Moiseyev, Light Stops at Exceptional Points, Phys. Rev. Lett. **120**, 013901 (2018).
  - [159] X.-L. Zhang, S. Wang, B. Hou, and C. T. Chan, Dynamically Encircling Exceptional Points: In situ Control of Encircling Loops and the Role of the Starting Point Phys. Rev. X **8**, 021066 (2018).
  - [160] K. Ding, G. Ma, Z. Q. Zhang, and C. T. Chan, Experimental Demonstration of an Anisotropic Exceptional Point, Phys. Rev. Lett. **121**, 085702 (2018).
  - [161] L. Jin and Z. Song, Incident Direction Independent Wave Propagation and Unidirectional Lasing, Phys. Rev. Lett. **121**, 073901 (2018).
  - [162] Biorthogonal norms of the eigenstates are unaffected under the imaginary gauge field, see Supplemental Material A.
  - [163] L. Ge, Anomalous Minimum and Scaling Behavior of Localization Length Near an Isolated Flat Band, Ann. Phys. (Berlin) **529**, 1600182 (2017).
  - [164] For system  $b$ ,  $\mathcal{SP} = \sigma_x \otimes \sigma_y$  and  $U_{\mathcal{SP}} = P_{2n} \otimes \sigma_y$  in Eq. (2), where  $\otimes$  is the Kronecker product, and  $P_{2n}$  is a 90 degrees rotation of the  $2n \times 2n$  identical matrix  $I_{2n}$ .
  - [165] K. Takata and M. Notomi, Photonic Topological Insulating Phase Induced Solely by Gain and Loss, Phys. Rev. Lett. **121**, 213902 (2018).
  - [166] K. Sun, W. V. Liu, A. Hemmerich, and S. Das Sarma, Topological semimetal in a fermionic optical lattice, Nat. Phys. **8**, 67 (2012).
  - [167] J. M. Hou, Hidden-Symmetry-Protected Topological Semimetals on a Square Lattice, Phys. Rev. Lett. **111**, 130403 (2013).
  - [168] If the asymmetric intracell coupling  $\mu$ - $\nu$  at system boundary vanishes instead of the intercell coupling  $t_2$ , the conclusion for the existence of zero edge states is inverse as in the regions  $t_1^2 < \gamma^2 - t_2^2$  and  $t_1^2 > \gamma^2 + t_2^2$ .
  - [169] M. Creutz, End States, Ladder Compounds, and Domain-Wall Fermions, Phys. Rev. Lett. **83** 2636 (1999).

**SUPPLEMENTAL MATERIAL FOR “BULK-BOUNDARY CORRESPONDENCE IN A  
NON-HERMITIAN SYSTEM IN ONE DIMENSION WITH CHIRAL-INVERSION SYMMETRY”**

L. Jin and Z. Song

*School of Physics, Nankai University, Tianjin 300071, China*

**A. Imaginary gauge field and non-Hermitian Aharonov-Bohm effect**

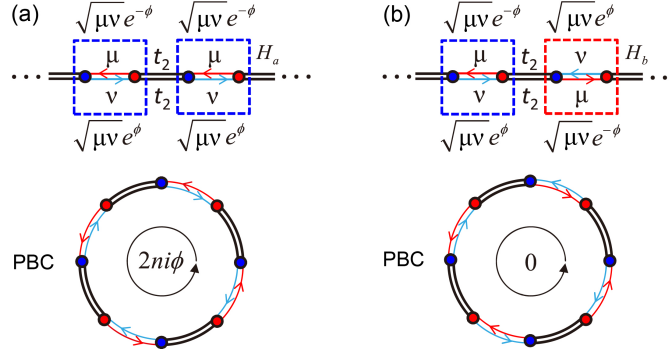


FIG. 5. Schematic of the imaginary gauge field and the magnetic flux. In the present of imaginary gauge field, particles or photons circling one round accumulate an amplification and attenuation factor  $e^{\pm 2n\phi}$  ( $0$ ) in opposite directions in system  $a$  ( $b$ ) under PBC; the enclosed imaginary magnetic flux is  $2ni\phi$  ( $0$ ). Under OBC, imaginary magnetic flux vanishes. The system size is  $N = 4n$ .

In Fig. 5, we show the systems with asymmetric coupling amplitudes are equivalent to systems with symmetric coupling amplitudes that associate with amplification and attenuation factors for tunneling in opposite directions. The amplification and attenuation factors  $e^{\pm\phi} = e^{\pm i\Phi}$  with  $\Phi = -i\phi$  indicates an imaginary gauge field  $\phi$ . The imaginary gauge field enclosed in an area induces a nonzero imaginary magnetic flux, which is a non-Hermitian Aharonov-Bohm (AB) effect. For system  $a$  under periodical boundary condition (PBC),  $e^{\pm\phi}$  accumulates along the translationally invariant direction; the accumulated factor in one circle is  $e^{\pm 2n\phi}$  for system size  $N = 4n$ . The enclosed imaginary magnetic flux is  $2n(i\phi)$  [Fig. 5(a)]. In contrast, the accumulated factor  $e^{\pm\phi}$  and  $e^{\mp\phi}$  in the blue cell and the red cell cancel each other in the compound four-site unit cell due to the chiral-inversion symmetry; this indicates that the imaginary magnetic flux does not exist in the chiral-inversion symmetric system  $b$  under PBC [Fig. 5(b)].

For  $\mu\nu > 0$ , the Bloch Hamiltonian of system  $a$  is

$$H_a(k) = \begin{pmatrix} 0 & \mu + t_2 e^{-ik} \\ \nu e^\phi + t_2 e^{ik} & 0 \end{pmatrix} = \begin{pmatrix} 0 & \sqrt{\mu\nu} e^{-\phi} + t_2 e^{-ik} \\ \sqrt{\mu\nu} e^\phi + t_2 e^{ik} & 0 \end{pmatrix}, \quad (9)$$

where  $e^{-\phi} = \sqrt{\mu/\nu}$  and  $\phi$  is an effective imaginary gauge field. Under the basis  $\{e^{-\phi} a_k^\dagger, b_k^\dagger\}$ , we have  $H_a(k)$  rewritten in the form of

$$H_a(k) = \begin{pmatrix} 0 & \sqrt{\mu\nu} + t_2 e^{-i(k+i\phi)} \\ \sqrt{\mu\nu} + t_2 e^{i(k+i\phi)} & 0 \end{pmatrix}. \quad (10)$$

The changing of basis indicates the implementation of a similar transformation, which does not vary the energy spectrum. Then,

$$H_a(k) = [\sqrt{\mu\nu} + t_2 \cos(k+i\phi)]\sigma_x + t_2 \sin(k+i\phi)\sigma_y. \quad (11)$$

The energy bands are  $E_{a,\pm} = \pm \sqrt{t_2^2 + \mu\nu + 2t_2\sqrt{\mu\nu} \cos(k+i\phi)}$ .

For  $\mu\nu < 0$ , the Bloch Hamiltonian of system  $a$  can be similarly rewritten in the form of symmetric coupling associated with an effective imaginary gauge field that induces amplification/attenuation factor  $e^{\pm\phi}$ . In the case of  $\mu < 0$  and  $\nu > 0$ , we have  $\mu = (i\sqrt{|\mu\nu|})(i\sqrt{|\mu/\nu|})$ ,  $\nu = (i\sqrt{|\mu\nu|})(-i\sqrt{|\nu/\mu|})$ , thus we set  $e^{-\phi} = i\sqrt{|\mu/\nu|}$ . In the case

of  $\mu > 0$  and  $\nu < 0$ , we have  $\mu = (i\sqrt{|\mu\nu|})(-i\sqrt{|\mu/\nu|})$ ,  $\nu = (i\sqrt{|\mu\nu|})(i\sqrt{|\nu/\mu|})$ , thus we set  $e^{-\phi} = -i\sqrt{|\mu/\nu|}$ . In both cases, we obtain

$$H_a(k) = \begin{pmatrix} 0 & i\sqrt{|\mu\nu|} + t_2 e^{-i(k+i\phi)} \\ i\sqrt{|\mu\nu|} + t_2 e^{i(k+i\phi)} & 0 \end{pmatrix}, \quad (12)$$

under the basis  $\{e^{-\phi} a_k^\dagger, b_k^\dagger\}$ .

Notably, under OBC, the imaginary gauge field is not enclosed; therefore, the imaginary magnetic flux vanishes and the amplification/attenuation factor  $e^{\pm\phi}$  does not affect the system spectrum. Consequently, systems  $a$  and  $b$  under OBC have identical spectra because the symmetric coupling amplitude  $\sqrt{\mu\nu}$  ( $\mu\nu > 0$ ) or  $i\sqrt{|\mu\nu|}$  ( $\mu\nu < 0$ ) without amplification/attenuation  $e^{\pm\phi}$  in system  $a$  is identical with that of system  $b$ . This alternatively proves the identical spectra of systems  $a$  and  $b$  under OBC. For instance, the Hamiltonians of a four-site systems  $a$  and  $b$  under OBC, and the four-site Hamiltonian with symmetric coupling  $\sqrt{\mu\nu}$  are

$$H_{a,4} = \begin{pmatrix} 0 & \mu & 0 & 0 \\ \nu & 0 & t_2 & 0 \\ 0 & t_2 & 0 & \mu \\ 0 & 0 & \nu & 0 \end{pmatrix}, H_{b,4} = \begin{pmatrix} 0 & \mu & 0 & 0 \\ \nu & 0 & t_2 & 0 \\ 0 & t_2 & 0 & \nu \\ 0 & 0 & \mu & 0 \end{pmatrix}, H_{S,4} = \begin{pmatrix} 0 & \sqrt{\mu\nu} & 0 & 0 \\ \sqrt{\mu\nu} & 0 & t_2 & 0 \\ 0 & t_2 & 0 & \sqrt{\mu\nu} \\ 0 & 0 & \sqrt{\mu\nu} & 0 \end{pmatrix}. \quad (13)$$

We can easily check that they have identical eigenvalues of  $E_{\pm,\pm} = \pm(t_2/2) \pm \sqrt{(t_2/2)^2 + \mu\nu}$ .

The right eigenstate of  $H_{a,4}$  ( $H_{b,4}$ )  $|\psi_{a,4}\rangle_R = [e^{-\phi}f_1, f_2, f_3, e^\phi f_4]^T$  ( $|\psi_{b,4}\rangle_R = [f_1, e^\phi f_2, e^\phi f_3, f_4]^T$ ) relates to the right eigenstate of  $H_{S,4}$   $|\psi_{S,4}\rangle_R = [f_1, f_2, f_3, f_4]^T$  with the same eigenvalue under a gauge transformation. The left eigenstate [109] of  $H_{a,4}$  ( $H_{b,4}$ )  ${}_L\langle\psi_{a,4}| = [e^\phi f_1^*, f_2^*, f_3^*, e^{-\phi} f_4^*]$  ( ${}_L\langle\psi_{b,4}| = [f_1^*, e^{-\phi} f_2^*, e^{-\phi} f_3^*, f_4^*]$ ) relates to the left eigenstate of  $H_{S,4}$   ${}_L\langle\psi_{S,4}| = [f_1^*, f_2^*, f_3^*, f_4^*]$  with the same eigenvalue [ ${}_L\langle\psi_{S,4}| = (|\psi_{S,4}\rangle_R)^\dagger$  in Hermitian systems]. The biorthogonal norms of the eigenstates ( ${}_L\langle\psi_{a,4}|\psi_{a,4}\rangle_R = {}_L\langle\psi_{b,4}|\psi_{b,4}\rangle_R = {}_L\langle\psi_{S,4}|\psi_{S,4}\rangle_R$ ) are identical, but the Dirac norms ( ${}_R\langle\psi_{a,4}|\psi_{a,4}\rangle_R \neq {}_R\langle\psi_{b,4}|\psi_{b,4}\rangle_R \neq {}_R\langle\psi_{S,4}|\psi_{S,4}\rangle_R$ ) are different.

## B. The inverse participation ratio of the bulk states

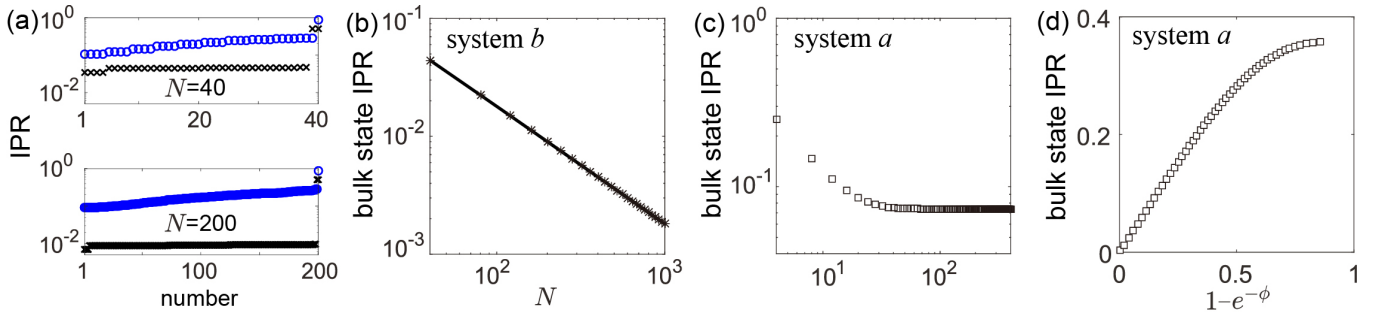


FIG. 6. (a) IPR of all the eigenstates, the blue circles (black crosses) are for system  $a$  (b). (b) Averaged IPR for all the bulk states of system  $b$ , which scales as  $1/N$ . The system parameters are  $t_1 = 1/4$ ,  $\gamma = 1/2$ , and  $t_2 = 1$  in (a, b). (c) Averaged IPR for all the bulk states of system  $a$ ,  $t_1 = 1$ ,  $\gamma = 1/8$ , and  $t_2 = 1$ . (d) Averaged IPR for all the bulk states of system  $a$  at large system size  $N = 400$  as a function of imaginary gauge field at  $t_1 = t_2 = 1$ ,  $e^{-\phi} = \sqrt{\mu/\nu}$ ,  $\mu = t_1 - \gamma$ , and  $\nu = t_1 + \gamma$ .

The inverse participation ratio (IPR)  $\sum_j |\psi_j|^4$  (with normalization  $\sum_j |\psi_j|^2 = 1$ ) for the eigenstates of system  $a$  (blue circles) is system size insensitive compared with IPR of system  $b$  (black crosses) in Fig. 6(a). Fig. 6(b) depicts the averaged IPR for the bulk eigenstates of system  $b$ , which is inversely proportional to the system size  $\text{IPR} \propto N^{-1}$ ; this reflects that all the bulk states of system  $b$  is extended state.

In Fig. 6(c), the averaged IPR of system  $a$  is depicted for weak non-Hermiticity. Correspondingly, the imaginary gauge field strength is weak. It is noticed that at small system size, the bulk states still exhibits the property of the extended states ( $\text{IPR} \propto N^{-1}$ ); in contrast, at large system size, the boundary localization effect of bulk states appears, the averaged IPR is insensitive to system size. The averaged IPR at large system size is a function of the attenuation factor  $e^{-\phi}$  [Fig. 6(d)], linearly increases as  $(1 - e^{-\phi})$  at weak non-Hermiticity and is bounded at strong non-Hermiticity that leads to strong localization of the bulk states at the system boundary.



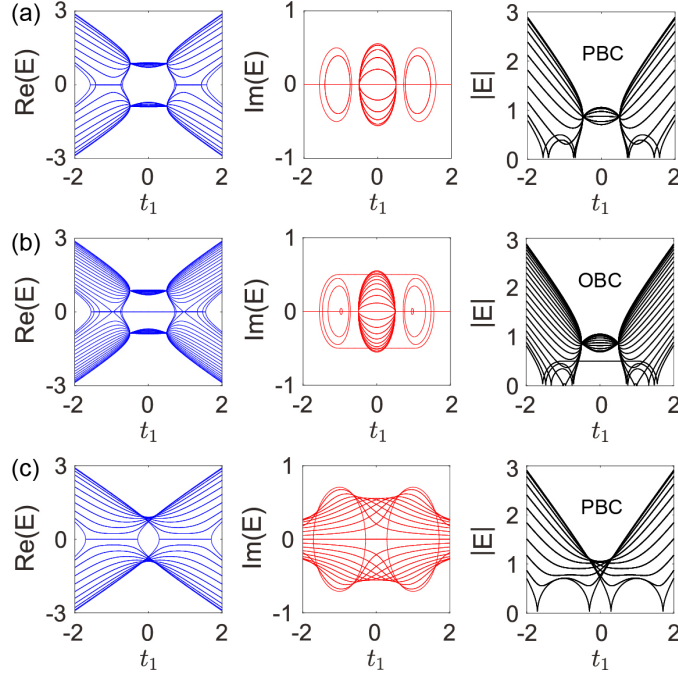


FIG. 7. Energy spectrum for system  $b$  with staggered gain and loss  $\{i\Gamma, -i\Gamma, i\Gamma, -i\Gamma\}$  under (a) PBC and (b) OBC. (c) Energy spectrum for system  $a$  with staggered gain and loss  $\{i\Gamma, -i\Gamma\}$  under PBC. The corresponding OBC spectrum is in (b). The parameters are  $N = 40$ ,  $\gamma = 1/2$ ,  $\Gamma = 1/2$ , and  $t_2 = 1$ .

### E. Topological characterization

The bulk-boundary correspondence is valid for the chiral-inversion symmetric system  $b$  due to the absence of nonzero imaginary magnetic flux. The bulk Bloch Hamiltonian of system  $b$  characterizes the topological properties of system  $b$  and the (non)existence of edge states under OBC; the topological invariant is a Bloch topological invariant for system  $b$ . The bulk Bloch Hamiltonian of system  $b$  also characterizes the topological properties of system  $a$  under OBC because the identical spectra of systems  $b$  and  $a$  under OBC. However, the bulk-boundary correspondence is invalid due to the lack of chiral-inversion symmetry in system  $a$ ; the bulk Bloch Hamiltonian of system  $a$  is not able to characterize the (non)existence of edge states in system  $a$  under OBC. Thus, the topological invariant is a non-Bloch topological invariant for system  $a$ .

In system  $b$ , the bulk topological properties relate to the (non)existence of edge states. Here we calculate the bulk topological invariant of system  $b$ , which is capable of characterizing the topologies of both systems  $a$  and  $b$  under OBC. The Bloch Hamiltonian of system  $b$  is a  $4 \times 4$  matrix; after a similar transformation, the Bloch Hamiltonian can be expressed in the form of  $\vec{B} \cdot \vec{\sigma}$  with a two-site unit cell, then we define a vector field  $\mathbf{F}(\mathbf{k})$  that is associated with the Bloch Hamiltonian. The topological defects with vortices or antivortices in the vector field indicate the phase transition points. The vorticity of the topological defects is a topological invariant. We consider that  $t_1$  and  $\gamma$  are real numbers,  $\mu = t_1 - \gamma$  and  $\nu = t_1 + \gamma$ , discussions on other cases are similarly following the same procedure below.

For  $\mu\nu > 0$ ,  $\mu$ ,  $\nu$ , and  $\sqrt{\mu\nu}$  are positive real numbers. The Bloch Hamiltonian  $H_b(k)$  under a similar transformation  $U_{\mu\nu>0} = \text{diag}(\sqrt{\nu}, \sqrt{\mu}, \sqrt{\mu}, \sqrt{\nu})$  that only consists of diagonal elements, yields

$$U_{\mu\nu>0} H_b(k) U_{\mu\nu>0}^{-1} = \begin{pmatrix} 0 & \sqrt{\mu\nu} & 0 & t_2 e^{-ik} \\ \sqrt{\mu\nu} & 0 & t_2 & 0 \\ 0 & t_2 & 0 & \sqrt{\mu\nu} \\ t_2 e^{ik} & 0 & \sqrt{\mu\nu} & 0 \end{pmatrix}, \quad (22)$$

which equals to the Bloch Hamiltonian of chiral-inversion symmetric system  $b$  with the imaginary gauge field  $\pm i\phi$  removed. The eigenvalues are symmetric  $E_{b,\pm,\pm} = \pm \sqrt{t_2^2 + \mu\nu} \pm 2t_2 \sqrt{\mu\nu} \cos(k/2)$ . In the discrete system with lattice size  $N = 4n$ , the wave vector  $k$  is  $k = 2\pi m/n$ ,  $m \in [1, n]$  ( $m, n$  are positive integers) for the Bloch Hamiltonian with a four-site unit cell. The Bloch Hamiltonian of equation (22) also equals to system  $a$  with all the asymmetric

couplings  $\mu$  and  $\nu$  replaced by the symmetric coupling  $\sqrt{\mu\nu}$  and taken two unit cells as a compound unit cell. The Bloch Hamiltonian of equation (22) is rewritten in the form of

$$h_b(k) = \begin{pmatrix} 0 & \sqrt{\mu\nu} + t_2 e^{-ik} \\ \sqrt{\mu\nu} + t_2 e^{ik} & 0 \end{pmatrix}. \quad (23)$$

$h_b(k) = \vec{B} \cdot \vec{\sigma}$ , where the effective magnetic field is

$$\vec{B} = (\sqrt{\mu\nu} + t_2 \cos k, t_2 \sin k, 0). \quad (24)$$

Notably, the wave vector  $k$  is  $k = \pi m/n$ ,  $m \in [1, 2n]$  for the Bloch Hamiltonian with a two-site unit cell.

We define a vector field  $\mathbf{F}(\mathbf{k}) = (\langle \sigma_x \rangle, \langle \sigma_y \rangle)$  to characterize the topology of  $h_b(k)$ . The eigenstates associated with  $E_{\pm}(k) = \pm \sqrt{(\sqrt{\mu\nu} + t_2 e^{-ik})(\sqrt{\mu\nu} + t_2 e^{ik})}$  are

$$\psi_{\pm}(k) = \frac{1}{\sqrt{2\sqrt{\mu\nu} + 2\sqrt{\mu\nu}t_2 \cos k + t_2^2}} \begin{pmatrix} \pm \sqrt{\sqrt{\mu\nu} + t_2 e^{-ik}} \\ \sqrt{\sqrt{\mu\nu} + t_2 e^{ik}} \end{pmatrix}. \quad (25)$$

The average values of the Pauli matrices associated with the two-component effective magnetic field  $\langle \sigma_{x,y} \rangle_{\pm} = \langle \psi_{\pm}(k) | \sigma_{x,y} | \psi_{\pm}(k) \rangle$  are

$$\langle \sigma_x \rangle_{\pm} = \frac{\pm(\sqrt{\mu\nu} + t_2 \cos k)}{\sqrt{\mu\nu + 2\sqrt{\mu\nu}t_2 \cos k + t_2^2}}, \quad \langle \sigma_y \rangle_{\pm} = \frac{\pm t_2 \sin k}{\sqrt{\mu\nu + 2\sqrt{\mu\nu}t_2 \cos k + t_2^2}}, \quad (26)$$

i.e.,  $(\langle \sigma_x \rangle_{\pm}, \langle \sigma_y \rangle_{\pm}) = (B_x, B_y)/E_{\pm}$ ; thus,  $(\langle \sigma_x \rangle_{\pm}, \langle \sigma_y \rangle_{\pm})$  reflects the topological properties of the Bloch bands and the system. The vector field  $\mathbf{F}(\mathbf{k})$  under either eigenstate yields the same winding number  $w = \oint_L (2\pi)^{-1} (\hat{F}_x \nabla \hat{F}_y - \hat{F}_y \nabla \hat{F}_x) d\mathbf{k}$  in the parameter plane  $\mathbf{k} = (k, t_2)$ , where  $\hat{F}_{x(y)} = F_{x(y)}/\sqrt{F_x^2 + F_y^2}$  and  $\nabla = \partial/\partial \mathbf{k}$ . The phase transition occurs at  $(k, t_2) = (0, -\sqrt{\mu\nu})$  or  $(\pm\pi, \sqrt{\mu\nu})$ , which are the band touching degeneracy points. They are topological defects in the vector field possessing integer topological charges (vortices and antivortices) as depicted in Fig. 3(a) in the main paper. The winding number  $w$  characterizing the vorticity of the topological defects, is a topological invariant.

For  $\mu\nu < 0$ ,  $-\mu$ ,  $\nu$ , and  $\sqrt{-\mu\nu}$  are positive real numbers. The Bloch Hamiltonian  $H_b(k)$  under a similar transformation  $U_{\mu\nu < 0} = \text{diag}(\sqrt{\nu}, i\sqrt{-\mu}, i\sqrt{-\mu}, \sqrt{\nu})$ , yields

$$U_{\mu\nu < 0} H_b(k) U_{\mu\nu < 0}^{-1} = \begin{pmatrix} 0 & i\sqrt{-\mu\nu} & 0 & t_2 e^{-ik} \\ i\sqrt{-\mu\nu} & 0 & t_2 & 0 \\ 0 & t_2 & 0 & i\sqrt{-\mu\nu} \\ t_2 e^{ik} & 0 & i\sqrt{-\mu\nu} & 0 \end{pmatrix}, \quad (27)$$

which is the Bloch Hamiltonian of system *a* with all the asymmetric couplings  $\mu$  and  $\nu$  replaced by the symmetric coupling  $i\sqrt{-\mu\nu}$  and taken two unit cells as a compound unit cell. The Bloch Hamiltonian can be rewritten as

$$h_b(k) = \begin{pmatrix} 0 & i\sqrt{-\mu\nu} + t_2 e^{-ik} \\ i\sqrt{-\mu\nu} + t_2 e^{ik} & 0 \end{pmatrix}, \quad (28)$$

where the effective magnetic field is

$$\vec{B} = (i\sqrt{-\mu\nu} + t_2 \cos k, t_2 \sin k, 0). \quad (29)$$

the eigenvalues are  $E_{\pm}(k) = \pm \sqrt{(i\sqrt{-\mu\nu} + t_2 e^{-ik})(i\sqrt{-\mu\nu} + t_2 e^{ik})}$ ; correspondingly, the eigenstates are

$$\psi_{\pm}(k) = \frac{1}{\sqrt{\Delta}} \begin{pmatrix} \pm \sqrt{i\sqrt{-\mu\nu} + t_2 e^{-ik}} \\ \sqrt{i\sqrt{-\mu\nu} + t_2 e^{ik}} \end{pmatrix}, \quad (30)$$

where  $\Delta = \sqrt{t_2^2 - 2\sqrt{-\mu\nu}t_2 \sin k - \mu\nu} + \sqrt{t_2^2 + 2\sqrt{-\mu\nu}t_2 \sin k - \mu\nu}$ .



The average values of  $\langle \sigma_{x,y} \rangle_{\pm} = \langle \psi_{\pm}(k) | \sigma_{x,y} | \psi_{\pm}(k) \rangle$  are

$$\langle \sigma_x \rangle_{\pm} = \frac{\pm \left( \sqrt{e^{-2ik} t_2^2 - \mu\nu} + \sqrt{e^{2ik} t_2^2 - \mu\nu} \right)}{\Delta}, \quad \langle \sigma_y \rangle_{\pm} = \frac{\pm i \left( \sqrt{e^{-2ik} t_2^2 - \mu\nu} - \sqrt{e^{2ik} t_2^2 - \mu\nu} \right)}{\Delta}. \quad (31)$$

The phase transition points are  $(k, t_2) = (\pm\pi/2, \pm\sqrt{-\mu\nu})$ , which are the band touching EPs. They are topological defects in the vector field possessing half-integer topological charges (vortices and antivortices) as depicted in Fig. 3(b) in the main paper.

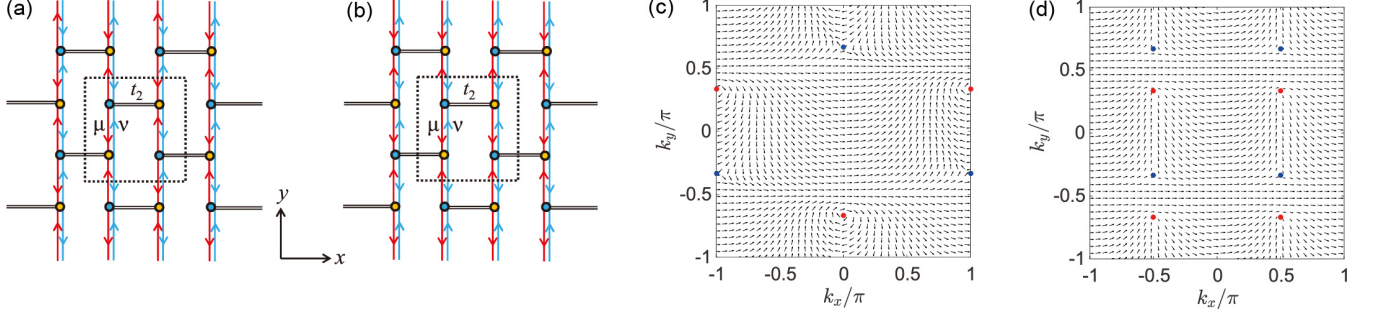


FIG. 8. (a, b) Schematic of the 2D brick wall lattice. The 2D lattices in the  $x$ -direction are the 1D non-Hermitian SSH lattices in Fig 1 of the main paper, respectively. (c, d) The vector field  $\mathbf{F}(k_x, k_y)$  associated with the  $E_{b,+}^{(2D)}$  state. The parameters are  $t_2 = 1$  and (c)  $\mu\nu = 1$ , (d)  $\mu\nu = -1$ .

The two-dimensional (2D) brick wall lattices are schematically illustrated in Figs. 8(a) and 8(b), along one direction of the 2D lattices are systems  $a$  and  $b$ , respectively. In the momentum space, the Bloch Hamiltonians  $H_a^{(2D)}(k)$  and  $H_b^{(2D)}(k)$  are

$$H_a^{(2D)}(k) = \begin{pmatrix} 0 & 2\mu \cos(k_y) & 0 & t_2 e^{-ik_x} \\ 2\nu \cos(k_y) & 0 & t_2 e^{ik_x} & 0 \\ 0 & t_2 e^{-ik_x} & 0 & 2\mu \cos(k_y) \\ t_2 e^{ik_x} & 0 & 2\nu \cos(k_y) & 0 \end{pmatrix}, \quad (32)$$

$$H_b^{(2D)}(k) = \begin{pmatrix} 0 & 2\mu \cos(k_y) & 0 & t_2 e^{-ik_x} \\ 2\nu \cos(k_y) & 0 & t_2 e^{ik_x} & 0 \\ 0 & t_2 e^{-ik_x} & 0 & 2\nu \cos(k_y) \\ t_2 e^{ik_x} & 0 & 2\mu \cos(k_y) & 0 \end{pmatrix}. \quad (33)$$

The vortices and antivortices associated with the phase transition points in the Brillouin zone in the  $k_x - k_y$  space are shown in Figs. 8(c) and 8(d), which are in accord with that revealed in Figs. 3(a) and 3(b) in the main paper.

Under a similar transformation  $U_b^{(2D)} = \text{diag}(\sqrt{\nu}, \sqrt{\mu}, \sqrt{\mu}, \sqrt{\nu})$ , the Bloch Hamiltonian  $H_b^{(2D)}(k)$  changes into

$$U_b^{(2D)} H_b^{(2D)}(k) U_b^{(2D)-1} = \begin{pmatrix} 0 & 2\sqrt{\mu\nu} \cos k_y & 0 & t_2 e^{-ik_x} \\ 2\sqrt{\mu\nu} \cos k_y & 0 & t_2 e^{ik_x} & 0 \\ 0 & t_2 e^{-ik_x} & 0 & 2\sqrt{\mu\nu} \cos k_y \\ t_2 e^{ik_x} & 0 & 2\sqrt{\mu\nu} \cos k_y & 0 \end{pmatrix}, \quad (34)$$

and the corresponding two-site unit cell Bloch Hamiltonian is

$$h_b^{(2D)} = \begin{pmatrix} 0 & 2\sqrt{\mu\nu} \cos k_y + t_2 e^{-ik_x} \\ 2\sqrt{\mu\nu} \cos k_y + t_2 e^{ik_x} & 0 \end{pmatrix}, \quad (35)$$

where the eigenvalues are  $E_{b,\pm}^{(2D)} = \pm \sqrt{t_2^2 + 4\sqrt{\mu\nu} \cos k_x \cos k_y + 4\mu\nu \cos^2 k_y}$ .

## F. Energy spectra for complex asymmetric coupling

For system  $b$  at  $\gamma = \sqrt{1/2}e^{i\pi/4}$ , the phase transition points are  $t_1 = \pm \sqrt[4]{3/4} \approx 0.93$  and  $|\cos(k)| = \sqrt{(2 + \sqrt{3})}/2$ . The band touching degeneracy points may not be seen in the discrete system with small system size due to the finite number of discrete  $k$ . The energy spectra for  $\gamma = \sqrt{1/2}e^{i\pi/4}$  are depicted in Fig. 9 for  $N = 40$ .

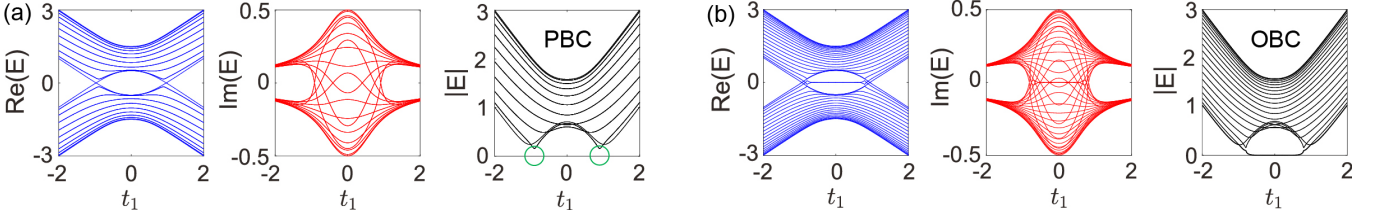


FIG. 9. Energy spectra of system  $b$  under (a) PBC and (b) OBC. The parameters are  $N = 40$ ,  $\gamma = \sqrt{1/2}e^{i\pi/4}$ , and  $t_2 = 1$ .

For system  $b$  at complex  $\gamma$ , the momenta  $k$  for band touching in the energy spectra are no longer  $0, \pm\pi/2$ , or  $\pm\pi$  and may not be seen in the discrete system with small size. The nonvanishing gap in  $|E|$  diminishes (vanishes) as system size increasing ( $N \rightarrow \infty$ ). The nonvanishing gap in  $|E|$  shown inside the green circles in Fig. 9(a) is a finite size effect of the discrete system; as  $N$  increases, the gap vanishes and the band touching degeneracy points reveal.

### G. Edge states for systems with a defective unit cell at boundary

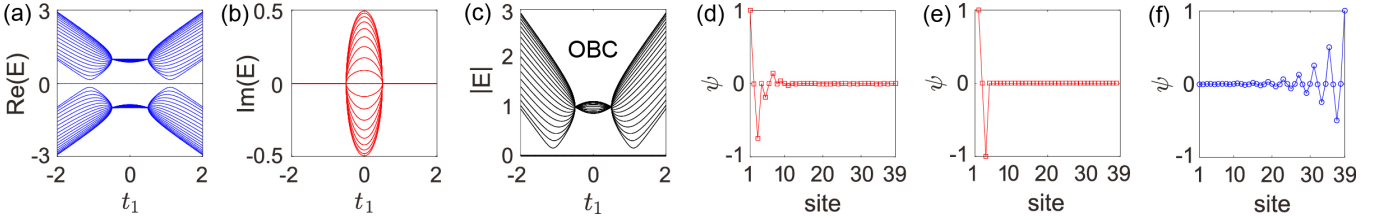


FIG. 10. (a-c) Energy spectra of system  $b$  with  $N = 39$  at parameters  $\gamma = 1/2$  and  $t_2 = 1$ . The zero edge state at (d)  $t_1 = 1/4$ , (e)  $t_1 = 1/2$ , and (f)  $t_1 = 3/2$ .

For system  $b$  with an even site number (total site number  $N = 4n - 2$ ), we consider that  $H_b$  under OBC with two sites (inside the red rectangle of chiral-inversion symmetric system  $H_b$  in Fig. 1 of the main paper) at the right boundary are missing. Two zero edge states localize at the left and the right boundaries, respectively. The left edge state is Eq. (5) in the main paper. The right edge state localized at the right boundary is  $\psi_{2j-1} = 0$  and

$$\psi_{N-2j} = -[(\nu + \mu) + (-1)^j (\nu - \mu)] / (2t_2) \psi_{N+2-2j}, \quad (36)$$

at large system size limit ( $N \gg 1$ ). For the anomalous edge states at the EPs ( $t_1^2 = \gamma^2$ ), they are localized at a single unit cell at system boundary. For  $t_1 = -\gamma$ , the left (right) edge state is  $\psi_1 = 1$  ( $\psi_N = 1$ ); and for  $t_1 = \gamma$ , the right edge state is  $\psi_N = 1$ ; the left edge state is  $\psi_1 = -(+)\psi_3 = 1$  for  $t_1/t_2 > 0$  ( $t_1/t_2 < 0$ ).

For system  $b$  with an odd site number, the energy spectra are depicted in Figs. 10(a)–10(c), the edge state is depicted in Figs. 10(d)–10(f). Only one zero edge state exists in this situation. If the unit cell at the right boundary is defective, in the situation that  $|\mu\nu| < t_2^2$ , the edge state localizes at the left boundary, the wave function is Eq. (5) in the main paper; in the situation that  $|\mu\nu| > t_2^2$ , for the system with site number  $N = 4n - 1$ , the edge state localized at the right boundary is  $\psi_{2j} = 0$  and

$$\psi_{N-2j} = -(2t_2) / [(\mu + \nu) + (-1)^j (\mu - \nu)] \psi_{N+2-2j}; \quad (37)$$

for the system with site number  $N = 4n - 3$ , the edge state localized at the right boundary is  $\psi_{2j} = 0$  and

$$\psi_{N-2j} = -(2t_2) / [(\nu + \mu) + (-1)^j (\nu - \mu)] \psi_{N+2-2j}. \quad (38)$$

For the anomalous edge states at the EPs ( $t_1^2 = \gamma^2$ ) and the systems with site numbers  $N = 4n - 1$  and  $4n - 3$ , the left edge state is  $\psi_1 = -(+)\psi_3 = 1$  for  $t_1/t_2 > 0$  ( $t_1/t_2 < 0$ ) at  $t_1 = \gamma$  and  $\psi_1 = 1$  at  $t_1 = -\gamma$ .

In contrast, for system  $a$  with an odd site number having a defective unit cell at the right boundary, only one zero state exists. The right boundary state is  $\psi_{2j} = 0$  and  $\psi_{N-2j} = (-t_2/\nu) \psi_{N+2-2j}$  when  $|t_2| < \sqrt{\mu\nu}$ . At the EPs, the zero state localizes at one site on the left boundary  $\psi_1 = 1$  for  $t_1 = -\gamma$ ; and the zero state is extended, being  $\psi_{2j} = 0$  and  $\psi_{2j-1} = -(+)\psi_{2j+1}$  for  $t_1 = \gamma$  at  $t_1/t_2 > 0$  ( $t_1/t_2 < 0$ ).

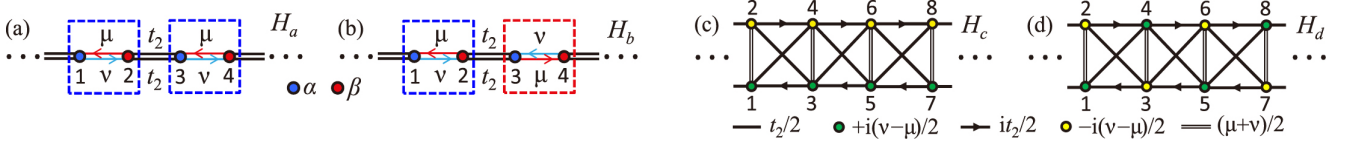


FIG. 11. (a, b) Schematic of the 1D SSH lattices, the unit cells are indicated in the squares. (c) and (d) are the equivalent non-Hermitian Creutz ladders of (a) and (b), respectively.  $H_\rho(k)$  ( $H_\rho$ ) is the Hamiltonian  $\rho$  in the  $k$ -space (real-space), where  $\rho = a, b, c, d$ . The system sizes are all  $N = 4n$ . This indicates that the imaginary gauge field relates to the real gauge field associated with balanced gain and loss.

## H. Equivalence between systems and their connections

The systems discussed have the total lattice size  $N = 4n$ , and the labels are marked in Fig. 11. In the real-space, through a unitary transformation

$$U = \frac{1}{\sqrt{2}} I_{2n} \otimes (i\sigma_x + I_2), \quad (39)$$

the systems  $a$  and  $b$  change into their corresponding quasi-1D Creutz ladder systems  $c$  and  $d$ , respectively; i.e.,  $H_{c(d)} = UH_{a(b)}U^{-1}$ ; where  $\otimes$  is the Kronecker product and  $I_{2n}$  is the  $2n \times 2n$  identical matrix. After the  $U$  transformation, the SSH chain with asymmetric coupling changes into the Creutz ladder in Fig. 4 of the main paper.

In the  $k$ -space, the Bloch Hamiltonians are

$$H_a(k) = \begin{pmatrix} 0 & \mu + t_2 e^{-ik} \\ \nu + t_2 e^{ik} & 0 \end{pmatrix}, H_c(k) = \frac{1}{2} \begin{pmatrix} i\nu - i\mu - 2t_2 \sin k & \mu + \nu + 2t_2 \cos k \\ \mu + \nu + 2t_2 \cos k & i\mu - i\nu + 2t_2 \sin k \end{pmatrix}, \quad (40)$$

$$H_b(k) = \begin{pmatrix} 0 & \mu & 0 & t_2 e^{-ik} \\ \nu & 0 & t_2 & 0 \\ 0 & t_2 & 0 & \nu \\ t_2 e^{ik} & 0 & \mu & 0 \end{pmatrix}, H_d(k) = \frac{1}{2} \begin{pmatrix} i\nu - i\mu & \mu + \nu & it_2(1 - e^{-ik}) & t_2(1 + e^{-ik}) \\ \mu + \nu & i\mu - i\nu & t_2(1 + e^{-ik}) & -it_2(1 - e^{-ik}) \\ -it_2(1 - e^{ik}) & t_2(1 + e^{ik}) & i\mu - i\nu & \mu + \nu \\ t_2(1 + e^{ik}) & it_2(1 - e^{ik}) & \mu + \nu & i\nu - i\mu \end{pmatrix}. \quad (41)$$

The Bloch Hamiltonians  $H_a(k)$  and  $H_c(k)$  are connected via  $U_{ac} = (i\sigma_x + I_2)$  as

$$U_{ac} H_a(k) U_{ac}^{-1} = H_c(k); \quad (42)$$

the Bloch Hamiltonians  $H_b(k)$  and  $H_d(k)$  are connected via  $U_{bd} = I_2 \otimes (i\sigma_x + I_2)$  as

$$U_{bd} H_b(k) U_{bd}^{-1} = H_d(k). \quad (43)$$

For the sake of comparison, the Bloch Hamiltonians of systems  $a$  and  $c$  are alternatively shown in form of

$$H'_a(k) = \begin{pmatrix} 0 & \mu & 0 & t_2 e^{-ik} \\ \nu & 0 & t_2 & 0 \\ 0 & t_2 & 0 & \mu \\ t_2 e^{ik} & 0 & \nu & 0 \end{pmatrix}, H'_c(k) = \frac{1}{2} \begin{pmatrix} i\nu - i\mu & \mu + \nu & it_2(1 - e^{-ik}) & t_2(1 + e^{-ik}) \\ \mu + \nu & i\mu - i\nu & t_2(1 + e^{-ik}) & -it_2(1 - e^{-ik}) \\ -it_2(1 - e^{ik}) & t_2(1 + e^{ik}) & i\nu - i\mu & \mu + \nu \\ t_2(1 + e^{ik}) & it_2(1 - e^{ik}) & \mu + \nu & i\mu - i\nu \end{pmatrix}, \quad (44)$$

where two unit cells are considered as a compound one,  $U_{bd} H'_a(k) U_{bd}^{-1} = H'_c(k)$ . In the discrete systems with lattice size  $N = 4n$ , the wave vector  $k$  is  $k = \pi m/n$ ,  $m \in [1, 2n]$  ( $m, n$  are positive integers) for the Bloch Hamiltonians  $H_a(k)$  and  $H_c(k)$  with a two-site unit cell, and the wave vector  $k$  is  $k = 2\pi m/n$ ,  $m \in [1, n]$  for the Bloch Hamiltonians  $H'_a(k)$ ,  $H_b(k)$ ,  $H'_c(k)$ , and  $H_d(k)$  with a four-site unit cell. Notably,  $H_a(k)$  and  $H'_a(k)$  [ $H_c(k)$  and  $H'_c(k)$ ] yield identical energy bands.

## I. 2D non-Hermitian topological systems

The breakdown and recovery of conventional bulk-boundary correspondence are discussed for two 2D non-Hermitian topological systems. The Bloch Hamiltonian of a 2D non-Hermitian Chern insulator is given by

$$H_{a,CI}(k_x, k_y) = (m + t \cos k_x + t \cos k_y) \sigma_x + (t \sin k_x + i\gamma) \sigma_y + (t \sin k_y) \sigma_z. \quad (45)$$

Set  $\mu = m + t \cos k_y + \gamma$ ,  $\nu = m + t \cos k_y - \gamma$ , we obtain

$$H_{a,CI}(k_x, k_y) = \begin{pmatrix} t \sin k_y & \mu + te^{-ik_x} \\ \nu + te^{ik_x} & -t \sin k_y \end{pmatrix}. \quad (46)$$

The coupling  $\mu\nu$  is asymmetric for  $\gamma \neq 0$ . The energy bands are  $E_{a,CI,\pm} = \pm\sqrt{\mu\nu + t^2 + t^2 \sin^2 k_y + t(\mu e^{ik_x} + \nu e^{-ik_x})}$ , which can be rewritten as

$$E_{a,CI,\pm}(k_x, k_y) = \pm\sqrt{\mu\nu + t^2 + t^2 \sin^2 k_y + 2t\sqrt{\mu\nu} \cos(k_x + i\phi)}, \quad (47)$$

where  $\sqrt{\mu/\nu} = e^{-\phi}$  for  $\mu\nu > 0$  [in the case of  $\mu < 0$  and  $\nu > 0$ , we set  $e^{-\phi} = i\sqrt{|\mu/\nu|}$ ; in the case of  $\mu > 0$  and  $\nu < 0$ , we set  $e^{-\phi} = -i\sqrt{|\mu/\nu|}$ ]. In both cases, we obtain the energy bands by replacing  $\sqrt{\mu\nu}$  with  $i\sqrt{|\mu\nu|}$  in Eq. (47)]. From the energy bands, we notice that a nonzero imaginary magnetic flux exists in the  $x$  direction; thus, the bulk-boundary correspondence fails in the  $x$  direction [130]. A chiral-inversion symmetry in the  $y$  direction can be defined for the non-Hermitian Chern insulator  $a$ , which does not prevent the nonzero imaginary magnetic flux in the  $x$  direction.

To recover conventional bulk-boundary correspondence, we can enforce an inversion symmetry when introducing the non-Hermiticity (asymmetric coupling) in the Chern insulator. Then, the bulk Bloch Hamiltonian is given by

$$H_{b,CI}(k_x, k_y) = \begin{pmatrix} t \sin k_y & \sqrt{\mu\nu}e^{-\phi} & 0 & te^{-ik_x} \\ \sqrt{\mu\nu}e^{\phi} & -t \sin k_y & t & 0 \\ 0 & t & t \sin k_y & \sqrt{\mu\nu}e^{\phi} \\ te^{ik_x} & 0 & \sqrt{\mu\nu}e^{-\phi} & -t \sin k_y \end{pmatrix}. \quad (48)$$

The Bloch Hamiltonian  $H_{b,CI}(k_x, k_y)$  has zero imaginary magnetic flux under PBC because of the cancellation between amplification and attenuation factors  $e^{\pm\phi}$  in the  $x$  direction. A chiral-inversion symmetry in the  $x$  direction can be defined for the non-Hermitian Chern insulator  $b$ . After a gauge transformation  $U_{CI} = \text{diag}(e^{ik_x/2}, e^{ik_x/2}, 1, 1)$ , we obtain  $H'_{b,CI}(k_x, k_y) = U_{CI}H_{b,CI}(k_x, k_y)U_{CI}^{-1}$ , then  $(\mathcal{S}\mathcal{P})H'_{b,CI}(k_x, k_y)(\mathcal{S}\mathcal{P})^{-1} = -H'_{b,CI}(-k_x, k_y)$  is satisfied with  $\mathcal{S}\mathcal{P} = \sigma_y \otimes \sigma_y$ . By applying the procedure done for the SSH model with asymmetric coupling, we can obtain an equivalent bulk Bloch Hamiltonian through removing the imaginary gauge field (wiping off the amplification and attenuation factors  $e^{\pm\phi}$ ), which gives

$$h_{b,CI}(k_x, k_y) = \begin{pmatrix} t \sin k_y & \sqrt{\mu\nu} + te^{-ik_x} \\ \sqrt{\mu\nu} + te^{ik_x} & -t \sin k_y \end{pmatrix}. \quad (49)$$

The energy bands are

$$E_{b,CI,\pm}(k_x, k_y) = \pm\sqrt{\mu\nu + t^2 + t^2 \sin^2 k_y + 2t\sqrt{\mu\nu} \cos(k_x)}. \quad (50)$$

The bulk topology of  $h_{b,CI}(k_x, k_y)$  can correctly predict the topological phase transition and the (non)existence of edge states for both Chern insulators  $a$  and  $b$  under OBC.

The approach is applicable in a 2D Rice-Mele model studied in Ref. [122]. The Bloch Hamiltonian is given by

$$H_{a,RM}(k_x, k_y) = [t_1 + \delta \cos k_x + (t_1 - \delta \cos k_x) \cos k_y] \sigma_x + [(t_1 - \delta \cos k_x) \sin k_y + i\gamma/2] \sigma_y - (\Delta \sin k_x) \sigma_z. \quad (51)$$

Set  $\mu = t_1 + \delta \cos k_x + \gamma/2$ ,  $\nu = t_1 + \delta \cos k_x - \gamma/2$ , and  $\sqrt{\mu/\nu} = e^{-\phi}$  for  $\mu\nu > 0$ , we obtain

$$E_{a,RM,\pm} = \pm\sqrt{\mu\nu + (t_1 - \delta \cos k_x)^2 + \Delta^2 \sin^2 k_x + 2(t_1 - \delta \cos k_x) \sqrt{\mu\nu} \cos(k_y + i\phi)}. \quad (52)$$

In contrast to the non-Hermitian Chern insulator shown in Eq. (45), a nonzero imaginary magnetic flux exists in the  $y$  direction, but not in the  $x$  direction of the 2D Rice-Mele model. Thus, in the  $y$  direction, the PBC and OBC spectra considerably differ from each other and conventional bulk-boundary correspondence fails in the  $y$  direction [122]. By enforcing an inversion symmetry when introducing the non-Hermiticity (asymmetric coupling) in the system, the imaginary magnetic flux vanishes, the conventional bulk-boundary correspondence recovers in the  $y$  direction. The bulk Bloch Hamiltonian has zero imaginary magnetic flux and is given by

$$H_{b,RM}(k_x, k_y) = \begin{pmatrix} -\Delta \sin k_x & \sqrt{\mu\nu}e^{-\phi} & 0 & (t_1 - \delta \cos k_x) e^{-ik_y} \\ \sqrt{\mu\nu}e^{\phi} & \Delta \sin k_x & (t_1 - \delta \cos k_x) & 0 \\ 0 & (t_1 - \delta \cos k_x) & -\Delta \sin k_x & \sqrt{\mu\nu}e^{\phi} \\ (t_1 - \delta \cos k_x) e^{ik_y} & 0 & \sqrt{\mu\nu}e^{-\phi} & \Delta \sin k_x \end{pmatrix}. \quad (53)$$

The equivalent system is obtained through removing the imaginary gauge field. Then, we obtain

$$h_{b,RM}(k_x, k_y) = \begin{pmatrix} -\Delta \sin k_x & \sqrt{\mu\nu} + (t_1 - \delta \cos k_x) e^{-ik_y} \\ \sqrt{\mu\nu} + (t_1 - \delta \cos k_x) e^{ik_y} & \Delta \sin k_x \end{pmatrix}. \quad (54)$$

The energy bands are given by

$$E_{b,RM,\pm} = \pm \sqrt{\mu\nu + (t_1 - \delta \cos k_x)^2 + \Delta^2 \sin^2 k_x + 2(t_1 - \delta \cos k_x) \sqrt{\mu\nu} \cos(k_y)}. \quad (55)$$

The bulk topology of  $h_{b,RM}(k_x, k_y)$  can correctly predict the topological phase transition and the (non)existence of edge states for both Rice-Mele models  $a$  and  $b$  under OBC.